Characterization and origin of low-T willemite (Zn2SiO4) mineralization: the case of the Bou Arhous deposit (High Atlas, Morocco)

Flavien Choulet, Luc Barbanson, Martine Buatier, Richard James, Torsten Vennemann, Aomar Ennaciri, Mohamed Zouhair

▶ **To cite this version:**

HAL Id: insu-01366479

https://insu.hal.science/insu-01366479

Submitted on 2 Oct 2020

1 **Characterization and origin of low-T willemite (Zn_2SiO_4) mineralization: the**

2 **case of the Bou Arhous deposit (High Atlas, Morocco)**

3

4 Choulet Flavien[1], Barbanson Luc[2], Buatier Martine[1], Richard James[1], Vennemann

5 Torsten[3], Ennaciri Aomar[4], Zouhair Mohamed[4]

6

7 [1]: Chrono-Environnement, UMR6249, Université de Bourgogne Franche-

8 Comté/CNRS, Besançon, France

9 [2]: Institut des Sciences de la Terre d'Orléans, UMR7327, Université

10 d'Orléans/CNRS/BRGM, Orléans, France

11 [3]: Institut des Dynamiques de la Surface Terrestre, Université de Lausanne, Lausanne,

12 Switzerland

13 [4]: Managem Group, Casablanca, Morocco

14

15   Willemite (Zn_2SiO_4) usually reported in hypogene non-sulfide deposits is

16 described as the main ore mineral in the carbonate-hosted Bou Arhous zinc deposit.

17 This deposit is located in the High Atlas intracontinental range that formed during the

18 Tertiary. Based on a set of microscopic observations, it was possible to establish that

19 willemite replaces primary sphalerite. On the basis of cathodoluminescence imaging,

20 three successive generations of willemite are distinguished, with evidence of

21 dissolution-reprecipitation processes. Willemite is also variably enriched in Ge (up to

22 1000 ppm), while Ge contents lower than 100 ppm are reported in the primary sulfide

23 minerals. Depending on the willemite generation, this substitution was positively or

24 negatively correlated to the Zn-Pb substitution. According to the nature of zoning

25 (sector versus oscillatory), the incorporation of Ge was either controlled by

crystallographic factors or by the nature of the mineralizing fluids. Willemite is associated with other oxidation-related mineral species, like cerussite ($PbCO_3$), but is not in isotopic equilibrium and therefore not considered to be cogenetic. Oxygen isotope compositions support the formation of willemite at temperatures below 130 °C, from mixed meteoric and deeper, hydrothermal fluids. The formation of the High Atlas Belt during the Tertiary has contributed to the exhumation of the sulfide minerals and the development of vertical conduits for percolation of meteoric water and ascending hydrothermal fluids. In addition to a local contribution of silicate minerals of the host limestone, hydrothermal fluids probably transported Si and Ge that are incorporated in willemite.

Keywords: willemite, non-sulfide zinc ore deposit, cathodoluminescence, germanium, stable isotopes, Morocco

Introduction

Unconventional non-sulfide zinc deposits have been the focus of many studies during the last two decades (e.g. Boni and Mondillo 2015). In addition to an evaluation of their economic potential, efforts have been made to establish and update the classification of non-sulfide zinc ore deposits (e.g. Hitzman et al. 2003; Boni and Large 2003). Presently, it is accepted that several types of deposits are distinguished. The supergene deposits formed by weathering of primary sulfides at surface temperature (see a review in Boni and Mondillo 2015). The hypogene deposits include: i) primary hydrothermal high-temperature zinc silicate deposits (e.g. Vazante in Brazil, Monteiro et al. 2006; or Beltana in Australia, Groves et al. 2003); ii)

2

51 secondary metamorphosed deposits (e.g. Franklin and Sterling Hill in USA; Johnson

52 et al. 1990) and iii) secondary low-temperature (<100 °C) Zn carbonate deposits (e.g.

53 Angouran in Iran, Boni et al. 2007; Daliran et al. 2013).

54   The occurrence of willemite (Zn_2SiO_4) is generally considered to be testimony

55 of a formation at relatively hot conditions (between 200 and 300 °C) under oxidizing

56 and alkaline conditions (Brugger et al. 2003). However, the origin of willemite is

57 controversial (Pough 1941), as the geological features of numerous willemite-rich

58 deposits are considered to derive from low-temperature (< 100 °C) hydrothermal

59 processes or supergene weathering. The historical deposits of Belgium in the Namur-

60 Verviers Synclinorium district include carbonate-hosted willemite ores whose origin

61 remains disputed (Dejonghe 1998; Boni et al. 2005; Coppola et al. 2008). Based on

62 ore characteristics and fluid inclusions, Coppola et al. (2008) hypothesized that

63 willemite may result from low-temperature hydrothermal processes caused by

64 oxidizing fluids with high silica activities. In addition to hypogene/hydrothermal

65 willemite (Boni et al. 2011), supergene willemite directly replacing primary sphalerite

66 has been described in the Namibian and Zambian carbonate-hosted oxidized zinc

67 deposits. The crystal habits, together with the mineral association and the presence of

68 monophase fluid inclusions, support a meteoric origin of the mineralizing fluids or at

69 least low-temperature hydrothermalism (Terracciano 2008). However, the presence of

70 supergene willemite in such carbonate-hosted environments is clearly a paradox.

71 Smithsonite ($ZnCO_3$) or hydrozincite ($Zn_5(CO_3)_2(OH)_6$) are supposed to be stable in

72 the weathering zone (Reichert and Borg 2008). At 25 °C, willemite may precipitate

73 instead of smithsonite at low CO_2 fugacity (log f_{CO2}<-1.6) and in the presence of silica

74 (log a_{quartz}>-3) (Brugger et al. 2003). However, this model does not consider the

75 possibility to precipitate hemimorphite. According to McPhail et al. (2003; 2006),

76 hemimorphite is stable with respect to willemite at temperatures below 90-100 °C.

77 This may explain why hemimorphite ($Zn_4Si_2O_7(OH)_2 \cdot (H_2O)$) is frequently reported in

78 supergene deposits (Hitzman et al. 2003). Hence, the presence of willemite is

79 frequently explained by the direct precipitation from low-temperature hydrothermal

80 fluids (Coppola et al. 2008; Terracciano 2008).

81   Zinc silicate is a versatile luminescent mineral that has been widely used as a

82 phosphorescent agent in displays and lighting devices (Takesue et al. 2009). Based on

83 studies of natural Mn-rich samples from Franklin or Sterling Hill deposits, USA

84 (Palache 1935), it has been shown that Mn^{2+} guest ions are natural luminescence

85 activators in willemite, which emits in a green color (Bhalha and White 1972). Green

86 willemite has been reported from hypogene deposits (Monteiro et al. 2007; Boni et al.

87 2011), while willemite from presumed supergene or low-temperature ores luminesces

88 in dull to bright blue (Coppola et al. 2008; Terracciano 2008; Melcher et al. 2009).

89 Although the origin of the blue emission is not clearly established and probably due to

90 activator or quenching ions other than Mn^{2+}, cathodoluminescence (CL) imaging

91 enables to reveal the different mineralization stages and may be used as a tool to

92 discriminate the origin of willemite.

93   The Bou Arhous deposit in Morocco exposes a non-sulfide ore that

94 contributed to the infilling of a large karst developed in Jurassic limestone (Leblanc

95 1968). The mined ore mainly consists of willemite associated with supergene or karst-

96 related minerals (Choulet et al. 2014, 2015). Except for the primary sulfide

97 mineralization, no evidence of a later hydrothermal event or Si-rich fluid input has

98 been reported yet. In this study, we present a detailed investigation of the willemite

99 ore texture coupled with a determination of its major and trace element composition.

100   In addition, stable isotope composition of willemite and cerussite are used to constrain

101   the characteristics of the mineralizing fluids and discuss the origin of willemite ores.

102

103   **The Bou Arhous deposit**

104

105   The Bou Arhous deposit is located in the High Atlas range, in the Central-

106   Eastern part of Morocco (Fig. 1a). The High Atlas range results from Tertiary

107   intracontinental deformation related to the closure of the Tethys (Frizon de la Motte et

108   al. 2000). The range consists of a fold-and-thrust belt with narrow anticlinal ridges

109   and large synclinal plains. Folded units are mainly composed of Jurassic limestone

110   and marl sequences that were originally emplaced into a horst and graben system

111   related to the opening of the Tethyan and Atlantic oceans (Laville and Piqué 1991).

112   Tertiary thrusts, rooted in the Triassic shales, reactivated the Jurassic normal faults.

113   These faults delimited the horst and graben domains, characterized by contrasted

114   sedimentary infilling.

115   The Moroccan High Atlas range hosts hundreds of base metal deposits and

116   occurrences that belong to the circum-Mediterranean Zn-Pb province (Rouvier et al.

117   1995). Several periods of ore deposition were distinguished (Mouguina 2004; Choulet

118   et al. 2014; Charles et al. 2016): 1) the Lower Jurassic with the emplacement of

119   stratabound Zn-Pb-Fe sulfides, 2) the Middle Jurassic including Cu-Ni and Zn-Pb

120   mineralization genetically associated with mafic magmatism, and 3) the Tertiary,

121   characterized by the supergene evolution of the aforementioned Jurassic deposits. For

122   this latter case, the supergene enrichment was strongly controlled by tectonics, which

123   enabled the exhumation of deep sulfide lenses and the development of faults that

124   served as drains for descending meteoric waters (Choulet et al. 2014).

125   Hosted in one of the High Atlas anticlinal ridges (Fig. 1b), the Bou Arhous ore

126   deposit is enclosed in Lower Sinemurian massive limestone ($l_{1\text{-}2}m$), to the south of the

127   Grand Accident Fault, a syn-sedimentary normal fault that was inverted during the

128   Tertiary (Leblanc 1968). At the mine, the bedding is steep to vertical and even

129   overturned (Fig. 2a). The limestone has developed a 120-m thick karst that extends

130   over 18,000 m^2 (Fig. 1b); sinkholes and tunnels are filled with detrital and residual

131   clays (Buatier et al. 2016; Choulet et al. 2016). The mineralization consists of a

132   network of interconnected vertical veins that meet the karst cavities (Fig. 2b). The

133   width of the veins may reach up to 10 meters. A vertical zonation of the mineralogical

134   associations is given with preserved sulfide minerals (sphalerite and galena) at depth

135   and newly formed non-sulfide minerals towards the surface (Choulet et al. 2014).

136   The Bou Arhous deposit is currently mined by Managem and reserves have

137   been estimated at 250 kt, grading 16 % Zn and 4 % Pb. The non-sulfide ore is mainly

138   composed of willemite and minor smithsonite, hydrozincite and hemimorphite.

139   Remnant galena and cerussite are associated with willemite forming black aggregates

140   (Fig. 2c). This black ore is often embedded in various clayey materials (Fig. 2d). The

141   barren red clays are of residual and detrital origin, linked with the development of the

142   karst system, whereas the white to ochre zinc clays are newly formed after willemite

143   dissolution (Choulet et al. 2016). Ore is processed at the site of Guemassa, south of

144   Marrakech since 2002, using hydrometallurgy to produce a ZnO concentrate as the

145   final product. Leaching by H_2SO_4 allows zinc recovery from oxidized ores, whatever

146   the mineralogy of the raw material (zinc silicates, carbonates or hydrated phases, but

147   not sulfide minerals).

148

149   **Material and methods**

150

151   Sample preparation and microscopic observation

152

153   Hand samples of black ore were collected in the different mine levels and cut

154   to prepare a set of 30 polished thin-sections. Whole-rock powders were also used for

155   X-ray diffraction (XRD) measurements. Procedure and results may be found in

156   Choulet et al. (2016). A first optical investigation using a Leica DMRX petrographic

157   microscope was complemented by Scanning Electron Microscopy (SEM) at the

158   FEMTO-ST Institute (Université de Bourgogne Franche-Comté, France). Back-

159   scattered electron (BSE) imaging operated at 15 kV in low vacuum conditions was

160   combined with semi-quantitative analysis using Energy-Dispersive Spectrometers

161   (EDS). Cold cathodoluminescence (CL) observations using OPEA instrumentation

162   hosted at Chrono-Environnement (Université de Bourgogne Franche-Comté) were

163   made with an acceleration voltage of 18.5 ± 1.5 keV and a current of 350 ± 150 mA to

164   investigate zoning in willemite and establish relationships with other minerals.

165   Additional spectral analyses were performed with a Zeiss MCS CCD UV-NIR

166   spectrophotometer.

167

168   Micro-analyses

169

170   The major element composition of sphalerite, galena and willemite was

171   obtained by Electron Probe Micro-Analysis (EPMA), at University of Lausanne,

172   Switzerland, using a JEOL 8200 Superprobe equipped with five Wavelength

173   Dispersion Spectrometers (WDS). Carbon-coated polished thin-sections were

174   analyzed with a beam of 20 kV for sulfide minerals and 15 kV for willemite,

175 respectively, and a current of 10 nA. The resolution is ca. 1 μm. Oxides, silicates and

176 pure metals were used as standards. Only analyses between 97 and 103 wt% were

177 retained for discussion.

178   Complementary LA-ICP-MS measurements of the Ge content were made on a

179 quadripolar Agilent 7500 ICPMS coupled with a 193 nm excimer Resonetics M-50E

180 laser hosted at the Université Blaise-Pascal, Clermont-Ferrand, France. The laser was

181 set up to produce an energy density of ca. 4 J.cm^{-2} at a repetition rate of 2 Hz. The

182 laser spot size was 20 μm in diameter. The following isotopes were monitored: ^{29}Si,

183 ^{66}Zn, ^{67}Zn, ^{68}Zn, ^{70}Ge, ^{72}Ge, ^{73}Ge, ^{74}Ge and ^{76}Ge. The total acquisition time

184 (background and signal) was limited to 100 s for one spot. Data reduction was carried

185 out with Glitter software. Zinc content previously measured by EPMA was used as an

186 internal standard. By comparing the recalculated Si and the EPMA-measured Si, it

187 appears that ^{67}Zn is the most suitable isotope for calibration. NIST 610 and NIST 612

188 were used as external standards (Pearce et al., 1997). While ^{70}Ge and ^{76}Ge were not

189 considered due to interference with ^{70}Zn and Ar isotopes, no significant differences

190 were observed between the three other Ge isotopes. ^{72}Ge was probably

191 underestimated because of a possible interference with ^{56}Fe^{16}O. As the abundance of

192 ^{74}Ge (36.28%) largely exceeds that of ^{73}Ge (7.73%), ^{74}Ge was retained for the

193 quantification of Ge in willemite.

194

195 Stable isotope analyses

196

197   Stable isotope analyses of ore and host limestone were done at the University

198 of Lausanne. 11 willemite and 7 carbonate (cerussite, calcite and dolomite)

199 concentrates were separated from the 200 μm milled fraction by heavy liquid methods

200　using LST Fastfloat ® liquor and filters. Grains were further handpicked under a

201　binocular microscope. The purity of concentrates was checked by XRD and only

202　reflections corresponding to cerussite or willemite were observed in the respective

203　samples. Because of the small size of the crystals, it was not possible to separate the

204　different generations of willemite and cerussite and only bulk compositions are

205　provided.

206　　　　O_2 was extracted from willemite by using a CO_2-laser line linked to a Finnigan

207　MAT 253 spectrometer. Between 1.5 to 2.5 mg of sample was loaded onto a small Pt-

208　sample holder and pumped out to a vacuum of about 10^{-6} mbar. After pre-fluorination

209　of the sample chamber, the samples were heated with a CO_2-laser in the presence of

210　50 mbar of pure F_2. Excess F_2 was separated from the O_2 produced by conversion to

211　Cl_2 using KCl held at 150 °C. The extracted O_2 was then introduced into the inlet of a

212　mass spectrometer. The detailed procedure may be found in Kasemann et al. (2001).

213　Oxygen isotope compositions are given in the standard δ-notation, expressed relative

214　to the Vienna Standard Mean Ocean Water (VSMOW) in permil (‰). Replicate

215　oxygen isotope analyses of the LS-1 in-house quartz standard had an average

216　precision of ± 0.03 ‰ (n = 5) for $\delta^{18}O$ and all values are normalized to a value of 9.64

217　‰ for NBS-28 quartz with an average accuracy better than 0.2 ‰.

218　　　　The C and O isotopic composition of carbonates was determined using a

219　GasBench II automated system interfaced to a Thermo Finnigan Delta PlusXL mass

220　spectrometer. The procedure is adapted after Spötl and Vennemann (2003). Oxygen

221　isotope analyses were corrected using the phosphoric acid fractionation at 70°C for

222　calcite (1.10087; Swart et al. 1991), for dolomite (1.0099; Rosenbaum and Sheppard

223　1986) and cerussite (1.00911; Gilg et al. 2003). The data are reported in the

224　conventional δ-values as ‰ deviations relative to the Vienna Pee Dee Belemnite

225   (VPDB) standards for C isotopes and to the VSMOW for O isotopes. Replicate

226   isotope analyses of the in-house standard used (CM) had an average precision of ±

227   0.04 ‰ for δ^{13}C and ± 0.07 ‰ for δ^{18}O (n = 4).

228

229   **Results**

230

231   Host rock and ore characterization

232

233   The host rock of the Bou Arhous mineralization is a massive fine-grained grey

234   to bluish-grey limestone. This micritic limestone locally includes coarse fragments of

235   echinoderms and lamellibranchs (Leblanc 1968). Idiomorphic quartz crystals are

236   frequently found in the micritic limestone as well as secondary sparite (Fig. 3a).

237   Despite a general euhedral shape, quartz grains often display a skeleton-like aspect,

238   suggesting dissolution (Fig. 3a), with evidence of late sparite precipitated in the newly

239   formed porosity. In addition, the bulk composition of the massive limestone has high

240   MgO contents (up to 13 wt%) that can be explained by a pervasive dolomitization

241   also revealed by XRD patterns (Choulet et al. 2016). Cathodoluminescence imaging

242   shows large dolomite crystals luminescing red within the micrite (Fig. 3b). In some

243   cases, dolomite may be altered and replaced by calcite. Small cavities or sinkholes are

244   filled with sparite with yellow luminescence (Fig. 3c). At the edge of the cavity, an

245   accumulation of dolomite rhombs and idiomorphic quartz is observed (Fig. 3c). This

246   stack of insoluble minerals differs from their random distribution in the preserved

247   micritic facies.

248   According to the XRD results, the ore is composed of willemite, cerussite,

249   galena and clays, associated with calcite, quartz and dolomite from the gangue and the

250   host rocks (Choulet et al. 2014; 2016). Remnant sulfide minerals include sphalerite

251   and galena. In thin-sections, corroded sphalerite can be seen as embedded in willemite

252   (Figs. 4a and 4g) and secondary galena (Gn II) has precipitated onto the rim of partly

253   dissolved sphalerite or along fractures cutting euhedral sphalerite (Figs. 4b and 4h).

254   Like the host micrite, willemite includes idiomorphic quartz crystals, exposing

255   fractures and evidence of corrosion (Fig. 4b). An irregular rim of anglesite locally

256   coats the galena (Gn I) and is itself transformed into cerussite (Fig. 4c). Frequently,

257   only granular cerussite that armors galena is observed and this assemblage often

258   constitutes the core of the euhedral willemite crystals (Figs. 4d and 4e). This latter

259   type of cerussite (Cer I) must not be mistaken for the late tabular crystals of cerussite

260   (Cer III) observed in the druses (Fig. 4e). Clusters of thin tabular crystals of barite are

261   found in association with willemite and cerussite (Figs. 4f to 4h) or as late

262   overgrowths within the geodes. Two types of willemite crystals have been found in all

263   thin-sections. While small barrel-shaped crystals are found in the equigranular ore

264   facies (Fig. 4d), radial-fibrous aggregates locally form a botryoidal facies (Fig. 5a). In

265   both cases, willemite crystals may display an irregular outline suggesting dissolution,

266   with zinc clays growing over willemite and filling the newly formed porosity (Fig.

267   5b). These clay minerals associated with detrital quartz (Fig. 5c) correspond to the

268   white clayey material that encompasses the willemite ore (Fig. 2d); they were

269   described in detail by Buatier et al. (2016) and Choulet et al. (2016). Radial-fibrous

270   willemite aggregates seem to postdate early cerussite (Cer I, often associated with Gn

271   I) and predate late cerussite infilling (Cer III, without galena) (Figs. 5d and 5e). In

272   addition, cerussite (Cer II) bands are intercalated between the different stages of

273   willemite growth (Fig. 5f).

274   As outlined above, several morphotypes of willemite may be found. This

275   includes: 1) idiomorphic barrel-shaped crystals (Fig. 6a), which are frequently

276   twinned (Fig. 6b) and 2) radial-fibrous aggregates or spherulites (Figs. 6c and 6d).

277   These crystal types must not be confused with the successive generations of willemite

278   that are described in the following section.

279

280   Identification of willemite generations

281

282   CL imaging was used for deciphering the successive generations of willemite.

283   The Bou Arhous willemite luminesces in blue from dull indigo to bright greenish-

284   blue. Three successive generations were distinguished:

285   -   Willemite Ia (Wil Ia), which partly refers to the prismatic morphotype (Fig.

286   6a) is characterized by sectoral zoning with sectors identified by their

287   luminescence (Fig. 7a). Deep indigo sectors seem to be associated with

288   particular faces, whilst bright blue sectors correspond to other faces. When

289   crystals display penetration twinning, pseudo-patchy zoning with an irregular

290   dark and bright chessboard pattern is observed. The extreme stage of multiple

291   twinning corresponds to the second morphotype of willemite, spherulites

292   (Figs. 6c and 6d), which exhibit a radial distribution of triangular dark sectors

293   separated by thin bright sectors (Fig. 7b).

294   -   Willemite Ib (Wil Ib) exhibits well-defined oscillatory zoning characterized by

295   a fine alternation of bright blue and dark indigo bands (Fig. 7b). Wil Ib always

296   develops on a core crystal, usually Wil Ia, with a sharp transition from sectoral

297   to oscillatory zoning (Figs. 7a and 7b). Individual willemite spherulites may

298   be merged to form aggregates, rimmed by banded willemite (Fig. 7c).

299   -   Willemite II (Wil II) corresponds to small grains that precipitate in the pores

300   between the aggregates of banded willemite or the willemite spherulites (Fig.

301   7d). They systematically form after a major dissolution stage affecting both

302   Wil Ia and Wil Ib, as evidenced by the convolute or truncated shape of crystals

303   (Figs. 7e and 7f). This dissolution stage is accompanied by the pervasive

304   development of thin interconnected fractures filled with cerussite (Figs. 7c and

305   7f) that luminesces in bright bluish white.

306

307   Composition of sulfide minerals and willemite

308

309   The mineral compositions of sulfides (galena and sphalerite) were obtained by

310   Electron Microprobe Analyzer (EPMA) and are given in Table 1. Sphalerite is poor in

311   Fe (<0.1 wt%) and minor elements were not detected. For galena, the minor element

312   content is low except for Ag, which may reach up to 0.3 wt%.

313   The composition of the different generations of willemite was obtained by

314   EPMA and LA-ICPMS methods and results are reported in Table 2. The total oxide

315   content averages 99 wt%, with a standard deviation between 0.3 and 0.6 wt%. The

316   major oxide content (ZnO and SiO_2) slightly varies (1 to 2 wt%) between the different

317   generations of willemite (Table 2). Willemite does not contain major impurities,

318   except for PbO that may reach up to 2 wt% (Table 2). No Mn was detected in the

319   different generations of willemite. The Ge content analyzed by LA-ICPMS was

320   compared to the Ge content recalculated from EPMA-measured GeO_2. Despite slight

321   differences, both datasets have the same trend and a similar range of element contents.

322   Significant differences between willemite sectors distinguished by CL imaging may

323   be noticed. While the dark sectors of Wil Ia have a low Ge content (less than 200

324 ppm) and a high PbO content (up to 2 wt%), the light sectors have significant Ge

325 contents with up to 1100 ppm (Figs. 8a and 8b). In both cases, the relative standard

326 deviation is low (Table 2). In contrast, the values for Ge in Wil Ib are irregularly

327 distributed with a range from 22 to 858 ppm and high standard deviation (Table 2).

328 Ablation spots were too large, compared to the growth bands of oscillatory-zoned

329 crystals (Fig. 8b). But, using EPMA, it was possible to analyze each band, and no

330 direct connection between the Ge content and the luminescence of the Wil-Ib crystals

331 are observed. The range for PbO content is between 0.06 and 0.84 wt% (Table 2). For

332 Wil II, the Ge content is below the detection limit and the PbO content ranges are

333 similar to those of other willemite generations.

334   In the individual Wil Ia crystals, a correlation between the Ge and Si contents

335 is marked by an extremely well-constrained trend line with a negative slope (Figs. 8c

336 and 8d). Despite an apparent random distribution, a similar trend is observed for all

337 data from Wil Ia and Wil Ib crystals (Fig. 8e). The Ge enrichment in willemite is

338 accompanied by a lower concentration of Si. When comparing the Zn and Pb

339 contents, differences between the different types of willemite are noted. While there is

340 no apparent correlation between Zn and Pb for Wil Ib, a well-defined trend with a

341 negative slope is observed for Wil Ia and Wil II (Fig. 8f).

342

343 Stable isotope compositions

344

345   Results of the stable isotope analyses on bulk willemite, bulk cerussite and

346 host carbonate samples are given in Table 3. For willemite, $\delta^{18}O$ values range from

347 5.3 to 7.8 ‰, except for sample BA136 ($\delta^{18}O$ = 15.6 ‰) that was contaminated by

348 the in-house quartz standard during laser extraction. While the $\delta^{18}O$ values of

349   cerussite are between 11.6 and 12.9 ‰, those of the limestone range from 22.9 to 24.1

350   ‰. Similarly, cerussite has low $\delta^{13}C$ values with a high variance (-11 to -15.1 ‰),

351   while the $\delta^{13}C$ values of host carbonates are between -1.7 and 1.4 ‰.

352

353   **Discussion**

354

355   Significance of the different willemite generations

356

357   Textures support three successive generations of willemite, with differences in

358   crystal shape, CL zoning and chemical composition. While idiomorphic Wil Ia is

359   characterized by sector zoning, radial-fibrous aggregates of Wil Ib have oscillatory

360   zoning and growth bands (Fig. 7). This textural evolution recalls that of the willemite

361   from ore deposits in Namibia, Zambia (Terracciano 2008), or Belgium (Coppola et al.

362   2008), where two distinct forms of willemite agglomerates were distinguished. These

363   authors described: 1) idiomorphic hexagonal crystals and 2) massive spheroids with

364   radial-fibrous crystals, which are very similar to Wil Ia and Wil Ib observed at Bou

365   Arhous, respectively. In the case of willemite, crystal shape is strongly controlled by

366   temperature (Palache 1935; Pough 1941) and by the degree of supersaturation

367   (Kostov 1968). Although accurate temperature constraints are missing, Kostov (1968)

368   has proposed that, at high temperature, crystals are usually tabular and as temperature

369   decreases, they tend to form elongated prisms along the c axis and, for extreme cases,

370   radial agglomerates of fibers. Kostov (1968) also proposed that a slow crystallization

371   from slightly supersaturated solutions could explain the short-prismatic to tabular

372   habits.

373   Based on a detailed microscopic observation of ore samples, we established

374   the temporal sequence of mineralization at Bou Arhous (Fig. 9). Primary sulfide

375   mineralization follows or at least overlaps the dolomitization and the silicification.

376   The latter alteration is marked by the development of authigenic quartz crystals in the

377   micritic limestone. Such quartz is usually found in carbonates affected by saline or

378   hypersaline pore waters (Flügel 2010); at Bou Arhous, the pore waters, from which

379   the authigenic quartz crystals precipitated, may result from the influence of the

380   underlying Triassic evaporites (Leblanc 1968). Cerussite predates and postdates

381   willemite precipitation (Fig. 9), as it may be found as core inclusions and cementing

382   material (*e.g*. Figs. 4d and 5e). Intercalation of cerussite bands within growth-zoned

383   willemite (Fig. 5f) supports the contemporaneity of both phases. Dissolution of

384   willemite was probably caused by a change in the local hydrochemical conditions (*i.e*.

385   Si-undersaturated fluids, change of temperature) and resulted in the release of zinc

386   and silica into the solutions, contributing to either a precipitation of a new generation

387   of willemite (Wil II) or the formation of authigenic zinc clays (Buatier et al. 2016;

388   Choulet et al. 2016)

389

390   Incorporation of Ge in willemite with implications for cathodoluminescence

391   properties

392

393   Both EPMA and LA-ICPMS analyses indicate a variable Ge content in

394   willemite that may reach up to 1000 ppm (Table 2). These values are significantly

395   higher than those measured in the New Jersey deposits (less than 10 ppm; Höll et al.

396   2007) and in the Utah and New Mexico deposits (up to 350 ppm; Sheffer 1966), but

397   are comparable to those reported from the Tsumeb Ge deposit, Namibia (up to 1280

398 ppm; Lombaard et al. 1986) or Tres Marias Zn-Pb-(Ge) deposit, Mexico (up to 4000

399 ppm; Saini-Eidukat et al. 2009; 2016). The EPMA results of this study clearly show a

400 correlation with a negative slope between Si and Ge, explained by the Ge-Si

401 substitution within willemite (Figs. 8d and 8e). X-ray absorption fine structure

402 (XAFS) spectroscopy has confirmed that Ge in willemite occurs as Ge^{4+} (Melcher et

403 al. 2009; Saini-Eidukat et al. 2016). The lithophile behavior of germanium (Bernstein

404 1985), the short difference in ionic radii between Ge^{4+} (0.44 Å) and Si^{4+} (0.39 Å) and

405 the similarity of lattice parameters between Zn_2SiO_4 and Zn_2GeO_4 (Hang et al. 1970)

406 may explain the incorporation of Ge into willemite.

407 Generally, sulfide minerals like sphalerite (e.g. Cook et al. 2009; Bélissont et

408 al. 2014) and galena (Monteiro et al. 2006) may contain several thousands of ppm of

409 Ge. At Bou Arhous, the Ge content of the two sulfide minerals is below the detection

410 limit (100 ppm) of EPMA (Table 1), in agreement with the low Ge content of MVT

411 deposits (Höll et al. 2007). Although the limited amount of sphalerite and galena

412 relics precludes implication for the whole primary mineralization, it means that either

413 an exceptional secondary Ge enrichment is recorded within willemite or that the

414 sulfide minerals were not the source of Ge. Except for the Apex mine where Ge

415 grades (ca. 5000 ppm) in the weathering zone exceed those in the primary sulfides

416 (650 ppm; Bernstein 1986), the oxidation zones of Zn–Pb sulfide deposits are

417 generally depleted in Ge or at least not enriched (Höll et al. 2007). In the Tres Marias

418 Deposit (Saini-Eidukat et al. 2009), the Ge content of sphalerite averages 960 ± 515

419 ppm and is comparable to that of willemite (941 ± 89 ppm). Ge can be transported in

420 aqueous hydrothermal fluids as $Ge(OH)_4°(aq)$ at pH values <8 over a temperature

421 range of 20 to 350 °C (Pokrovsky et al. 2005). In addition, the solubility of Ge in

422 thermal waters increases with temperature and salinity (Melcher et al. 2003). In this

423 case, the source of Ge could be organic-rich rocks (e.g. black shale), which are

424 generally rich in Ge (Bernstein 1985) and are frequent in the Paleozoic basement of

425 Morocco (Lüning et al. 2000). Hydrothermal fluids would therefore be necessary to

426 introduce the Ge for the willemite.

427   In addition to Ge, willemite has a variable Pb content that may reach up to 2

428 wt%, similar to the contents measured in Tres Marias willemite (Saini-Eidukat et al.

429 2009). By plotting Pb versus Zn, a correlation with a negative slope between both

430 elements is given, suggesting the existence of a Zn-Pb substitution (Fig. 8f), also

431 reported by Saini-Eidukat et al. (2016). According to XAFS spectroscopy, Pb is

432 present as Pb^{2+} in willemite (Melcher et al. 2009; Saini-Eidukat et al. 2016).

433 Willemite containing ca. 0.5 wt% of Pb^{2+} was synthetized by the sol-gel method with

434 calcination at 1000°C (Yang et al. 2004). Trigonal willemite is characterized by Zn-O

435 bonds (Kostov 1968); as the difference between the ionic radii of Zn^{2+} (0.60 Å) and

436 Pb^{2+} (0.98 Å) is huge, only a limited amount of Pb^{2+} may be introduced, with strong

437 distortion of the tetrahedrally coordinated site. Alternatively, the ring crystal structure

438 of willemite is characterized by tessellated hollow hexagons made of Si and Zn

439 tetrahedrons (Klaska et al. 1978; Lukić et al. 2008), which may incorporate interstitial

440 ions like Pb^{2+} (Yang et al. 2004). The relative incompatibility of Pb in willemite is

441 also shown by the existence of orthorhombic larsenite (Palache 1928; Ito and Frondel

442 1967), $ZnPbSiO_4$, and the absence of solid solution between larsenite and willemite.

443 Hence, Saini-Eidukat et al. (2016) have proposed that Pb-rich willemite may contain

444 microdomains of larsenite. In case of Pb supersaturation conditions related to a

445 change of the fluid composition, secondary galena or cerussite may be precipitated

446 (Terracciano 2008), as illustrated by the cerussite and galena inclusions in willemite

447 cores (Figs. 4d and 4e) and the intercalated cerussite bands (Fig. 5f).

448   Correlations between the two substitutions (Zn-Pb and Si-Ge) can be

449   observed, depending on the willemite generations (Fig. 10). In the case of Wil Ia, all

450   data except those with low Pb and low Ge contents are distributed along a trending

451   curve with a negative slope, which tends toward the Pb-rich compositions of

452   willemite. This indicates that significant Ge amounts can be included in this particular

453   willemite generation, only if that latter one is poor in Pb. As the Pb content increases,

454   the Ge-Si substitution is much more limited, probably due to the distortion of the

455   tetrahedrally coordinated site caused by the introduction of large Pb^{2+} ions (Saini-

456   Eidukat et al. 2016). In contrast, for Wil Ib, the curve has a positive slope, suggesting

457   that there is no competition between the two substitutions (Fig. 10). This trend is

458   similar to that of Tres Marias willemite, which is also characterized by well-

459   developed oscillatory zoning (Saini-Eidukat et al. 2009; 2016). In the case of Wil II,

460   the small number of data and the low Ge content precludes discussing incorporation

461   mechanisms. The differences between Wil Ia and Wil Ib may be explained by the

462   variation of crystal shapes (prismatic versus fiber-like) and, in the case of Wil Ia, by

463   the development of peculiar faces, which may incorporate more or less Ge and Pb at

464   the their surface during crystallization. A similar mechanism has been proposed to

465   explain sectoral chemical (Ge, Ag) zoning in sphalerite (Barbanson and Geldron

466   1983). According to Pough (1940) and Kostov (1968), the main faces of willemite

467   prisms are {110}, {101}, {012} and {001}. While the first one is characteristic of

468   fibrous habits (e.g. Wil Ib), the three other one are frequent in prismatic crystals (e.g.

469   Wil Ia). The comparison of the surface atomic structure of the different faces shows

470   that all faces except {012} display alternating Zn and Si, with various Si/Zn ratios.

471   However, the {012} surface is a continuous plane of Si ions, which was much more

472   favorable for Ge incorporation. Therefore, the incorporation of Ge in Wil Ia is limited

473   by willemite crystal growth, while its introduction in Wil Ib depends on the chemical

474   composition of the fluids, which controls the element variation of oscillatory-zoned

475   crystals (Shore and Fowler 1996). Oscillatory growth zoning in willemite is

476   frequently described in the literature (Coppola et al. 2008; Terracciano 2008; Saini-

477   Eidukat et al. 2009; 2016), but it is the first time that sector zoning is reported for this

478   mineral. Growth sectors defined by the faces on which the growth took place are

479   characterized by variable Ge and Pb contents (Fig. 8). While Ge-rich bright sectors

480   {012} have low Pb contents, higher Pb concentration is found in Ge-poor dark sectors

481   {101}, {110} or {001}.

482   Spectral analysis curves are characterized by a maximum of intensity at 460-

483   480 nm (Fig. 11), in agreement with the blue luminescence observed under the

484   microscope (Fig. 6). The experimental curves from Bou Arhous willemite

485   significantly differ from those given by pure willemite (Randall 1938; Yang et al.

486   2004) or Mn-doped willemite (Leverenz 1950), but are very similar to that obtained

487   by analyzing synthetic Zn_2GeO_4 nanorods (Tsai et al. 2008). Zinc germanate has a

488   crystal structure similar to that of willemite (Hang et al. 1970). The obvious

489   correlation between the Ge content and the intensity of luminescence is only valid for

490   Wil Ia crystals and no similar observation was made for Wil Ib. Therefore, it is

491   difficult to ascertain the role of activator ion for Ge^{4+}. Alternative processes could be

492   envisaged: (i) quenching by ions with intense charge transfer bands like Fe^{2+}

493   (Terracciano 2008), (ii) sensitizing of Mn by ions with intensive absorption bands like

494   Pb^{2+} (Carpenter and Vicenzi 2012), (iii) luminescence caused by defect activators,

495   such as interstitial Pb^{2+} (Yang et al. 2004; Takahashi et al. 2010), or (iv) other

496   luminescence centers (e.g. Ti^{4+}, Eu^{2+}, Ce^{3+}, Hf^{4+}) not detected by the used analytical

497 methods, but recognized as activators for the blue luminescence (see a review in

498 Takesue et al. 2009).

499

500 Nature of the mineralizing fluids involved

501

502 The host rock carbonates of the Bou Arhous mineralization have $\delta^{13}C$ values

503 in a range from -1.7 to 1.4 ‰ (Table 3), similar to those of Pliensbachian limestone

504 (0.5 to 2.9 ‰) hosting the Bou Dahar Zn-Pb mineralization, 75 km to the west of Bou

505 Arhous (Rddad and Bouhlel 2016). The $\delta^{18}O$ values of carbonates (22.9 to 24.1 ‰)

506 are also similar to those of Bou Dahar (22.7 to 25.7 ‰). Such $\delta^{13}C$ and $\delta^{18}O$ values

507 are within the range of marine Jurassic limestones (Veizer and Hoefs 1976).

508 Carbon stable isotope ratios of cerussite are similar to those measured for

509 supergene ores from Iglesiente, Broken Hill and deposits in Eastern Belgium (see a

510 review in Gilg et al. 2008; Fig. 12a). The $\delta^{13}C$ (between -11 and -15.1 ‰) values are

511 lower than the typical values of cerussite from marine slags (0 ± 2‰) given by Gilg

512 et al. (2008). The ^{13}C-depleted carbon component can be explained by either

513 contributions of carbon from soil CO_2 related to respiration of C3 plants (Cerling

514 1984) or organic carbon issued from the activity of sulfide-oxidation bacteria

515 (Melchiorre and Enders 2003). The average $\delta^{18}O$ value (12.1 ‰, n = 4) of cerussite is

516 lower than that obtained in supergene deposits (15 to 20 ‰) or from marine slags

517 (17.9 ‰, Gilg et al. 2008), but similar to that of the Garpenberg deposit, Sweden

518 (11.6 ‰; Vivallo and Broman 1993) or to that of Badenweiler in the Schwarzwald

519 mining district (11.2 to 15.6 ‰, Hassler et al. 2014). These low values may be

520 explained by either isotopically lighter water or by higher temperatures of formation.

521 The absence of any correlation between carbon and oxygen isotope values of cerussite

522   suggests that dissolution of the host limestone cannot only account for the source of

523   carbonate in cerussite.

524   At present, the oxygen isotope composition of willemite was only reported

525   from Sterling Hill (USA) and Vazante (Brazil), with respective isotopic compositions

526   between 7.4 ‰ and 11.4 ‰ and between 10.9 ‰ to 13.8 ‰ (Johnson et al. 1990;

527   Monteiro et al. 1999). In addition to fluid inclusions that recorded salinities of 3-15

528   wt% eq. NaCl and homogenization temperatures between 120 and 175°C (Dardenne

529   and Freitas-Silva 1999), Monteiro et al. (1999) recalculated a temperature range (from

530   263 to 294°C) at the time of mineralization using the stable isotope composition of

531   cogenetic mineral pairs. Therefore they recalculated the oxygen isotope composition

532   of the fluid in equilibrium with willemite, using the theoretical fractionation equation

533   between willemite and water (Zheng 1993).

534

535     $1000\ln\alpha_{\text{wil-wat}} = 3.79(10^6/T^2) - 8.94(10^3/T) + 2.5$ (*eq. 1*)

536

537   The range of oxygen isotope compositions ($\delta^{18}O$ = 12 to 14 ‰) of the fluid (Fig. 12b)

538   led Appold and Monteiro (2009) to propose a mixing process between hot, saline,

539   reducing, acidic fluids and cool, oxidizing meteoric waters; precipitation results from

540   an increase in pH and/or a small decrease in the temperature (Brugger et al. 2003).

541   Mixing of hydrothermal fluids with seawater was also hypothesized for explaining the

542   isotopic compositions of Sterling Hill rocks and ores (Johnson et al. 1990).

543   The oxygen isotope composition of Bou Arhous willemite is characterized by

544     $\delta^{18}O$ values ranging between 5.3 and 7.8 ‰ (Table 3), significantly lower than those

545   measured for Vazante or Sterling Hill. The large range of oxygen isotope values (2.5

546   ‰) may also indicate that fluid mixing was involved during the precipitation of

547 willemite or that willemite precipitated at different temperatures. The study of fluid

548 inclusions in willemite from Bou Arhous was not conclusive, with only monophase

549 inclusions observed. This suggests that the temperatures of the Tertiary fluids

550 responsible for willemite formation was below 130°C (e.g. Gilg et al. 2014). The

551 established paragenetic succession shows a first-order contemporaneity of willemite

552 and cerussite (Fig. 9). Using equation (*eq*. *1*) and the oxygen isotope fractionation

553 equation between cerussite and water (*eq*. *2*; Gilg et al. 2008), it is possible to

554 calculate the equilibrium temperature between the willemite-cerussite pairs (BA117,

555 BA118 and BA134).

556

557 $1000\ln\alpha_{cer-wat} = 2.29(10^6/T^2)-3.56$ (*eq*. *2*)

558

559 After discarding the negative solutions, the obtained temperatures range from

560 237 to 343°C. While these temperatures are similar to those proposed in hypogene

561 willemite deposits (e.g. Vazante; Monteiro et al. 1999), the local geological setting of

562 Bou Arhous deposit totally differs from the structural and paragenetic characteristics

563 of hypogene deposits, without carbonatization and hematite alteration (Hitzman et al.

564 2003). In addition, such temperatures are too high for cerussite, a mineral exclusively

565 reported in the supergene stages of ore deposits, although high temperature (up to 240

566 °C) experiments on cerussite were made by O'Neil et al. (1969). Cerussite and

567 willemite are not in isotopic equilibrium and thus not cogenetic. They precipitated

568 from at least two fluids with different oxygen isotope compositions or formed at

569 different temperatures. The successive bands of cerussite and willemite (Fig. 5f)

570 rather support the hypothesis of different fluids involved in the precipitation of both

571 minerals.

573   Supergene versus low-temperature hypogene willemite

574

575   Based on the present data, it is not possible to ascertain the origin of willemite

576 at Bou Arhous. The geological features of the deposits suggest a supergene origin of

577 the non-sulfide mineralization and therefore low temperatures (around 25 °C) could

578 be assumed. Such a temperature corresponds to that presently recorded in the karst

579 cavities hosting the mineralization. Synthetic willemite was obtained at room

580 temperature by sol-gel methods and occurs as small spheres or aggregates (Esquevin

581 1960; Takesue et al. 2009). Thermodynamic modeling also showed that willemite

582 may form at 25 °C under high pH, high silica activity and low CO_2 partial pressure

583 conditions (Brugger et al., 2003). The oxygen isotopic composition of the paleowater

584 was calculated at 25 °C, using the bond-strength theory equation for isotope

585 fractionation between willemite and water (eq. 1; Zheng 1993). The obtained isotopic

586 compositions for the paleowater (Table 3) plot close to the meteoric line (Craig 1961),

587 although no constrain on the vertical axis (δD) is available (Fig. 12b). The computed

588 $\delta^{18}O$ values for the paleofluid have a range between -9.3 ‰ and -7.4 ‰ (Table 3),

589 lower than the average value (-7.5 ‰) of present-day precipitations at Bab Bou Idir,

590 northern Morocco (Ouda et al. 2005). This difference could be explained by

591 differences in altitude and climate between the Bab Bou Idir station and the Bou

592 Arhous range during the Tertiary.

593   Alternatively, low-temperature hydrothermal fluids (<130°C) may have been

594 involved in the formation of willemite. Such fluids have been hypothesized for the

595 origin of willemite in the deposits of Eastern Belgium (Coppola et al. 2008). In the

596 case of Bou Arhous, the absence of isotopic equilibrium between cerussite and

24

597 willemite and the relatively large range of isotopic compositions for willemite suggest

598 the involvement of at least two fluids and their mixing. Together with supergene

599 water, hydrothermal fluids have also contributed to the formation of the non-sulfide

600 ore. As temperature is the main parameter controlling the precipitation of willemite

601 instead of hemimorphite (McPhail et al. 2003, 2006), temperatures over 90-100 °C are

602 required, in agreement with the presence of monophase inclusions (T <130 °C).

603 Assuming a temperature of 100 °C, we recalculated a range of isotopic compositions

604 for the paleofluid between -0.5 and 2 ‰ (Table 3). The data fall into an intermediate

605 domain between the deep fluid fields and the supergene line, in agreement with the

606 mixing hypothesis (Fig. 12b).

607 Whatever the hypothesis, high silica activity is necessary to prevent the

608 precipitation of smithsonite and hydrozincite, which are only reported in few samples

609 in the Bou Arhous deposit (Leblanc 1968). The source of silica is thus a crucial issue.

610 Like in Eastern Belgium (Coppola et al. 2008), few present-day hot springs are

611 currently known in the area, especially to the west of Bou Arhous (Bahaj et al. 2013).

612 In addition, the hydrochemical study of the underground waters in the Zizi and Guir

613 basins, to the south of the Bou Arhous range, shows that the present-day water within

614 the Sinemurian limestone is a calcic bicarbonate type; their extremely high silica

615 content (up to 5000 mg/L) are interpreted as the result of a long residence time of the

616 waters and/or an important mixture with thermal waters (Bahaj et al. 2013). A local

617 source for silica cannot be excluded too, and may even be indicated by the partial

618 dissolution of the idiomorphic quartz crystals present in the micritic limestone (Fig.

619 3). Although the dissolution rate of quartz is low at low temperatures (Dove 1994),

620 long-lived weathering since the Tertiary and undersaturation of the karst waters may

621 partly contribute to a slow but non-negligible enrichment in silica. An alternative

622 local source of Si could be the residual clays of the karst, mainly composed of illite,

623 kaolinite and smectite (Buatier et al. 2006; Choulet et al. 2016).

624

625 **Conclusion**

626

627   The Bou Arhous deposit in the Moroccan High Atlas is characterized by

628 willemite ore. Several generations of willemite spatially and temporally associated

629 with cerussite were distinguished based on different criteria including crystal shape,

630 zoning type and major and trace element contents. Based on oxygen stable isotope

631 data of bulk mineral fractions, cerussite and willemite are not in isotope equilibrium

632 and therefore were not cogenetic, requiring different fluid compositions for their

633 formation. In addition to a contribution of supergene water, low-temperature (<130

634 °C) hydrothermal fluids buffered by the country rocks may have been involved. The

635 input of hydrothermal fluids is probably responsible for the high silica activity, which

636 is necessary to precipitate willemite instead of zinc carbonates, especially within

637 carbonate host rocks. A local contribution by the silicate minerals of the host

638 limestone cannot be excluded though. Further work on willemite is required to verify

639 the conditions of formation; stable oxygen isotopes compositions of the different

640 generations of willemite and cerussite could help to understand the evolution of

641 mineralizing fluids.

642   The Bou Arhous willemite may contain up to several thousands ppm of Ge.

643 The Ge content in willemite, related to the Si-Ge substitution, is controlled by the

644 crystal morphology in the case of sector zoning. Since the Ge content of sulfide

645 minerals is low (less than 100 ppm), it is hypothesized that hydrothermal fluids,

646 responsible for the formation of willemite, also transported Ge in part. In the present

647 context of Ge criticality, willemite ores may therefore represent an interesting target

648 for exploration (Höll et al. 2007; EU Commission 2014).

649

650 **Acknowledgments**

651

664

665 **Figure captions**

666

667 Table 1 WDS results of the primary sulfide minerals (sphalerite and galena).

668 Detection limits (in ppm): S (320), Cd (100), As (210), Bi (900), Fe (110), Ag (460),

669 Ni (120), Zn (330), Pb (720), Ge (100), Cu (110). Avg: average, SD: standard

670 deviation, RSD: relative standard deviation (RSD = (SD/Avg.) * 100), n: number of

671 analyses, (-): values below the detection limit.

672

Table 2 WDS analyses (oxide in weight percent) and LA-ICPMS results (in ppm) of the different willemite generations described in the text. Detection limits (in ppm): Ge (84), Al (64), Pb (454), Cd (105), Fe (237), Ca (120), Mn (336). Avg: average, SD: standard deviation, RSD: relative standard deviation (RSD = (SD/Avg.) * 100), n: number of analyses, (n.d.): values below the detection limit.

678

Table 3 Stable isotope (C, O) compositions measured for cerussite, willemite and host limestone from the Bou Arhous deposit. For willemite, the oxygen isotopic composition of the fluid ($\delta^{18}O$ VSMOW$_f$) was calculated with the fractionation equation from Zheng (1993), assuming temperatures of 25 ([1]) and 100°C ([2]).

683

Figure 1 **a** Map of northwestern Africa, illustrating the location of the Bou Arhous deposits with respect to the major tectonic features. **b** Cross-section of the Bou Arhous deposit, showing the faulted anticline (adapted from Leblanc 1968). Triassic rocks (t) are covered by Lower Jurassic rocks (l_1 to l_4). The mine, made up of 4 levels (from level 0 to level 100) is hosted in massive limestone, to the south of the fault and mainly exposes a non-sulfide mineralization.

690

Figure 2 **a** Field image of the reddish thin-bedded folded limestone that alternates with marl. **b** General view of the southern flank of the Jbel Bou Arhous showing cavities originally filled by non-sulfide mineralization (Choulet et al. 2014). **c** and **d** Mine outcrops showing the "black ore" composed of galena and willemite, associated with zinc clays, detrital clays or hydrozincite.

696

697   Figure 3 Cathodoluminescence images of the host limestone. **a** Micrite (yellowish

698   pink) enclosing idiomorphic and partly dissolved quartz (blue), with locally secondary

699   sparite (yellow). **b** Dolomite (reddish pink) pervading into the micrite (yellowish

700   brown) and locally transformed into sparite (yellow). **c** Small sinkhole formed after

701   the dissolution of micrite (brown) and filled by sparite (yellow). Note the

702   accumulation of euhedral crystals of dolomite (pink) and quartz (blue) at the bottom

703   of the cavity.

704

705   Figure 4 Images of the ore mineralization. **a** General view (TL, nic+) of the willemite

706   (Wil) ore including relics of sphalerite (Sp) (Sample BA06C). **b** BSE image of (a)

707   showing sphalerite relic rimmed by secondary galena (Gn II), within willemite. Note

708   the idiomorphic quartz (Qz) crystals, partly corroded and fractured. **c** BSE image of

709   primary galena (Gn I) coated by a thin rim of anglesite (Ang) itself transformed into

710   cerussite (Cer I) (Sample BA05A). **d** (TL, nic+) and **e** (RL, nic//) Aggregates of

711   galena and cerussite (Cer I + Gn I) included within elongated willemite (Wil) crystals

712   (Sample BA06B). Large crystal of cerussite (Cer III) devoid of galena inclusions fills

713   the porosity between the willemite (Wil) aggregates. **f** (TL, nic+), **g** (TL, nic//) and **h**

714   (RL, nic//) Thin and tabular barite (Brt) crystals associated with willemite (Wil), late

715   cerussite (Cer III) and sphalerite (Sp), rimmed by secondary galena (Gn II) (Sample

716   BA06A). TL: transmitted light, BSE: backscattered elelectron, RL: reflected light,

717   nic+: crossed nicols, nic//: parallel nicols.

718

719   Figure 5 **a** Aggregate of willemite spherulites in the massive ore facies (TL, nic+)

720   (Sample BA135F). **b** (TL, nic+) and **c** (BSE image) Association of willemite with

721   newly formed zinc clays and detrital quartz, extensively described in Choulet et al.

722   (2016) (Sample BA130F). **d** (TL, nic+) and **e** (RL, nic//) General view of the different

723   generations of cerussite and relationships with the willemite spherulite (Sample

724   BA05B). **f** BSE image illustrating willemite spherulites postdating early cerussite (cer

725   I associated with primary galena relic) and predating late cerussite (cer III). Note the

726   cerussite band (cer II) intercalated during the growth of the spherulite. See Figure 4

727   for abbreviations.

728

729   Figure 6 Secondary electron images of separated willemite crystals, showing

730   idiomorphic barrel shape (**a**) (Sample BA124), twinning (**b**) (Sample BA133), and

731   radial-fibrous distribution (**c** and **d**) (Sample 134).

732

733   Figure 7 Cathodoluminescence images of the willemite ore. **a** Barrel-shaped crystals

734   showing a 1) core of Wil Ia with sector zoning and 2) a rim of Wil Ib with oscillatory

735   zoning (Sample BA130). **b** willemite spherulite composed by a core of Wil Ia mainly

736   composed of dark sectors, rimmed by oscillatory-zoned Wil Ib (Sample BA135F). **c**

737   aggregated spherulites showing a well developed Wil Ib stage (Sample BA128F).

738   Note the cerussite veins (bright white-blue) that crosscut Wil Ia and partly Wil Ib. **d**

739   Small crystals of late willemite (Wil II) filling the porosity between early willemite

740   (Wil Ia and Wil Ib) (BA135). **e** Partly dissolved willemite, exposing relics of an

741   oscillatory-zoned rim and dark sectors within the core. The bright zone in the center is

742   due to early cerussite (Sample BA128F). **f** Partly dissolved willemite spherulite

743   crosscut by cerussite veinlets (bright white-blue). Note on the upper right corner that

744   the sequence is probably repeated with time, as unaltered willemite with oscillatory

745   zoning overgrows on the dissolved spherulites (Sample BA128F).

746

747 Figure 8 Cathodoluminescence images of the willemite crystals, showing the location

748 of *in situ* point analyses by LA-ICPMS (**a** and **b**) and by EPMA (**c**). **d** Ge versus Si

749 plot of individual EPMA analyses located in fig. 8c. **e** Ge versus Si plot of all EPMA

750 analyses, including the distinguished willemite generations. **f** Pb versus Zn plot of all

751 EPMA analyses, including the distinguished willemite generations. The number of

752 Ge, Si, Zn and Pb moles was calculated from the weighted percent oxide

753 compositions reported in Table 2.

754

755 Figure 9 Synthetic paragenetic sequence of the observed minerals at the Bou Arhous

756 deposit. Vertical lines represent the limits between the different steps that contribute

757 to the present-day mineralization. Thickness of the horizontal line corresponds to the

758 relative abundance of each mineral species.

759

760 Figure 10 Ge/(Ge+Si) versus Pb/(Pb+Zn) plot illustrating that the two substitutions

761 (Ge-Si and Pb-Zn) are variably correlated depending on the willemite generation. The

762 data from willemite of Tres Marias deposit, Mexico (Saini-Eidukat et al. 2009) are

763 reported for comparison; these latter data show a trend similar to that of Wil Ib from

764 Bou Arhous.

765

766 Figure 11 Luminescence spectra of two observed areas dominated by Wil Ia or Wil

767 Ib. The curves of variously Mn-doped willemite (Leverenz 1950) and of a synthetic

768 Ge analog of willemite (Zn_2GeO_4, Tsai et al. 2008) are shown for comparison.

769

770 Figure 12 **a** Carbon and oxygen isotope compositions of cerussite and host limestone

771 from the Bou Arhous deposit. Data from other deposits are taken from Gilg et al.

772   (2008) and references herein. **b** Hydrogen and oxygen isotope compositions of

773   supergene (25 °C) and low-temperature (100 °C) hydrothermal fluids in equilibrium

774   with Bou Arhous willemite. The isotope composition of fluids in equilibrium with

775   hypogene willemite from Vazante, Brazil (Monteiro et al. 1999) is shown for

776   comparison.

777

778   **References**

779

780   Appold MS, Monteiro LVS (2009) Numerical modeling of the hydrothermal zinc

781   silicate and sulfide mineralization in the Vazante deposit, Brazil. Geofluids 9:96–115

782

783   Bahaj T, I. Kacimi I, Hilali M, Kassou N, Mahboub A (2013) Preliminary study of the

784   groundwater geochemistry in the sub-desert area in Morocco: case of the Ziz-Ghris

785   basins. Proced Earth Planet Sci 7:44–48

786

787   Barbanson L, Geldron A (1983) Distribution du germanium, de l'argent et du

788   cadmium entre les schistes et les minéralisations stratiformes et filoniennes à blende-

789   sidérite de la region de Saint-Salvy (Tarn). Chron Rech Min 470:33–42

790

791   Belissont R, Boiron M-C, Luais B, Cathelineau M (2014) LA-ICP-MS analyses of

792   minor and trace elements and bulk Ge isotopes in zoned Ge-rich sphalerites from the

793   Noailhac − Saint-Salvy deposit (France): Insights into incorporation mechanisms and

794   ore deposition processes. Geochim Cosmochim Acta 126:518–540

795

796   Bernstein LR (1985) Germanium geochemistry and mineralogy. Geochim

797   Cosmochim Acta 49:2409-2422

798

799   Bernstein LR (1986) Geology and mineralogy of the APEX germanium–gallium

800   mine, Washington County, Utah. US Geol Surv Bull 1577:1–9

801

802   Bhalla RJRSB, White EW (1972) Cathodoluminescence characteristics of Mn^{2+}

803   activated willemite (Zn_2SiO_4) single crystals . J Electrochem Soc 119:740–743

804

805   Boni M, Large DE (2003) Nonsulfide zinc mineralization in Europe: an overview.

806   Econ Geol 98:715–729

807

808   Boni M, Mondillo N (2015) The "calamines" and the "others": the great family of

809   supergene nonsulfide zinc ores. Ore Geol Rev 67:208– 233

810

811   Boni M, Coppola V, Dejonghe L, Fedele L (2005) Willemite in the Belgian non-

812   sulphide deposits: a fluid inclusion study. Period Miner 73:1–14

813

814   Boni M, Gilg HA, Balassone G, Schneider J, Allen CR, Moore F (2007) Hypogene

815   Zn carbonate ores in the Angouran deposit, NW Iran. Mineral Deposita 42:799–820

816

817   Boni M, Terracciano R, Balassone G, Gleeson SA, Matthews A (2011) The

818   carbonate-hosted willemite prospects of the Zambezi Metamorphic Belt (Zambia).

819   Mineral Deposita 46:707–729

820

821 Brugger J, McPhail DC, Wallace M, Waters J (2003) Formation of willemite in

822 hydrothermal environments. Econ Geol 98:819–835

823

824 Buatier M, Choulet F, Petit S, Chassagnon R, Vennemann T (2016) Nature and origin

825 of natural Zn clay minerals from the Bou Arhous Zn ore deposit: Evidence from

826 electron microscopy (SEM-TEM) and stable isotope compositions (H and O). App

827 Clay Sci, DOI: 10.1016/j.clay.2016.07.004

828

829 Carpenter P, Vicenzi E (2012) A combined EPMA and cathodoluminescence study of

830 minerals from Franklin NJ. Microsc Microanal 18(S2):1746–1747

831

832 Cerling TE (1984) The stable isotopic composition of modern soil carbonate and its

833 relationship to climate. Earth Planet Sci Letts 71:229–240

834

835 Charles N, Choulet F, Sizaret S, Chen Y, Barbanson L, Ennaciri A, Badra L, Branquet

836 Y (2016) Internal structures and dating of non-sulphide Zn deposits using rock

837 magnetism: insights from the Moroccan High Atlas. Mineral Deposita 51:151–175

838

839 Choulet F, Charles N, Barbanson L, Branquet Y, Sizaret S, Ennaciri A, Badra L, Chen

840 Y (2014) Non-sulfide zinc deposits of the Moroccan High Atlas: multi-scale

841 characterization and origin. Ore Geol Rev 56:115–140

842

843 Choulet F, Buatier M, Barbanson L, Guégan R, Ennaciri A (2016) Zinc-rich clays in

844 supergene non-sulfide zinc deposits. Mineral Deposita 51:467-490

845

846   Cook NJ, Ciobanu CL, Pring A, Skinner W, Shimizu M, Danyushevsky L, Saini-

847   Eidukat B, Melcher F (2009) Trace and minor elements in sphalerite: a LA-ICPMS

848   study. Geochim Cosmochim Acta 73:4761–4791

849

850   Coppola V, Boni M, Gilg HA, Balassone G, Dejonghe L (2008) The "calamine"

851   nonsulfide Zn–Pb deposits of Belgium: petrographical, mineralogical and

852   geochemical characterization. Ore Geol Rev 33: 187–210

853

854   Craig H (1961) Isotopic variations in meteoric waters. Science 133:1702–1703

855

856   Daliran F, Pride K, Walther J Berner ZA Bakker RJ (2013) The Angouran Zn (Pb)

857   deposit, NW Iran: evidence for a two stage, hypogene zinc sulfide–zinc carbonate

858   mineralization. Ore Geol Rev 53:373–402

859

860   Dardenne MA, Freitas-Silva FH (1999) Pb-Zn ore deposits of Bambuí and Vazante

861   groups, in the São Francisco Craton and Brasília Fold Belt, Brazil. In: Silva MG, Misi

862   A (eds) Base metal deposits of Brazil. MME7CPRM/DNPM, Belo Horizonte, pp. 75-

863   83

864

865   Dejonghe L (1998) Zinc-lead deposits of Belgium. Ore Geol Rev 12:329–354

866

867   Dove PM (1994) The dissolution kinetics of quartz in sodium chloride solutions at 25

868   degrees to 300 degrees C. Am J Sci 294:665–712

869

870 Esquevin J (1960) Les silicates de zinc, étude de produits de synthèse et des minéraux
871 naturels. Institut National de la Recherche Agronomique, Saint-Amand (in French)

872

873 EU Commission (2014) Critical raw materials for the EU. Report of the Ad-hoc
874 Working Group on Defining Critical Raw Materials. Brussels, Belgium

875

876 Flügel E (2010) Microfacies of Carbonate Rocks, 2nd edn. Springer-Verlag, Berlin-
877 Heidelberg

878

879 Frizon de Lamotte D, Saint-Bezar B, Bracene E, Mercier E (2000) The two main
880 steps of the Atlas building and geodynamics of the western Mediterranean. Tectonics
881 19:740–761

882

883 Gilg HA, Struck U, Vennemann T, Boni M (2003) Phosphoric acid fractionation for
884 smithsonite and cerussite between 25 and 72 °C. Geochim Cosmochim Acta 67:4049–
885 4055

886

887 Gilg HA, Boni M, Hochleitner R, Struck U (2008) Stable isotope geochemistry of
888 carbonate minerals in supergene oxidation zones of Zn–Pb deposits. Ore Geol Rev
889 33:117–133

890

891 Gilg HA, Krüger Y, Taubald H, van den Kerkhof AM, Frenz M, Morteani G (2014)
892 Mineralisation of amethyst-bearing geodes in Ametista do Sul (Brazil) from low-
893 temperature sedimentary brines: evidence from monophase liquid inclusions and
894 stable isotopes. Miner Deposita 49:861-877

895

896 Groves I, Carman CE, Dunlap WJ (2003) Geology of the Beltana willemite deposit,

897 Flinders Ranges, South Australia. Econ Geol 98:797–818

898

899 Hang C, Simonov MA, Belov NV (1970) Crystal structures of willemite $Zn_2(SiO_4)$

900 and its germanium analog $Zn_2(GeO_4)$. Sov Phys Crystallogr USSR 15:387–390

901

902 Hassler K, Taubald H, Markl G (2014) Carbon and oxygen isotope composition of

903 Pb-, Cu- and Bi-carbonates of the Schwarzwald mining district: Carbon sources, first

904 data on bismutite and the discovery of an oxidation zone formed by ascending thermal

905 water. Geochim Cosmochim Acta 113:1–16

906

907 Hitzman MW, Reynolds NA, Sangster DF, Allen CR, Carman CE (2003)

908 Classification, genesis, and exploration guides for nonsulfide zinc deposits. Econ

909 Geol 98:685–714

910

911 Höll R, Kling M, Schroll E (2007) Metallogenesis of germanium - A review. Ore

912 Geol Rev 30:145–180

913

914 Ito J, Frondel C (1967) Synthesis of lead silicates: larsenite, barysilite and related

915 phases. Am Mineral 52:1077-1084

916

917 Johnson CA, Rye DM, Skinner BJ (1990) Petrology and stable isotope geochemistry

918 of the metamorphosed zinc-iron-manganese deposit at Sterling Hill, New Jersey:

919 Econ Geol 85:1133–1161

920

921   Kasemann S, Meixner A, Rocholl A, Vennemann T, Schmitt A, Wiedenbeck M

922   (2001) Boron and oxygen isotope composition of certified reference materials NIST

923   SRM 610/612, and reference materials JB-2G and JR-2G. Geostand Newsl 25:405–

924   416

925

926   Klaska K-H, Eck JC, Pohl D (1978) New investigation of willemite. Acta Crystallogr

927   B34:3324–3325

928

929   Kostov I (1968) Habit types and genesis of phenakite and willemite. Krist Techn 3:

930   629–636

931

932   Laville E, Piqué A (1991) La distension crustale atlantique et atlasique au Maroc au

933   début du Mésozoïque: le rejeu des structures hercyniennes. Bull Soc Geol Fr

934   162:1161–1171

935

936   Leblanc M (1968) Étude géologique et métallogénique du Jbel Bou-Arhous et de son

937   prolongement oriental (Haut Atlas marocain oriental). Not Mem Serv Geol Maroc

938   206:117–206

939

940   Leverenz HW (1950) An introduction to luminescence of solids. John Wiley & Sons,

941   NewYork

942

943   Lombaard AF, Günzel A, Innes J, Krüger TL (1986) The Tsumeb lead-copper-zinc-

944   silver deposit, south west Africa/Namibia. In: Anhaeusser CR, Maske S (eds) Mineral

945   Deposits of Southern Africa. Geological Society of South Africa, Johannesburg, pp

946   1761–1787

947

948   Lukić DM, Petrović, Dramićanin MD, Mitrić M, Đaćanin L (2008) Optical and

949   structural properties of $Zn_2SiO_4:Mn^{2+}$ green phosphor nanoparticles obtained by a

950   polymer-assisted sol–gel method. Scr Mater 58:655-658

951

952   Lüning S, Loydell DK, Sutcliffe O, Ait Salem A, Archer R, Zanella E, Craig J, Harper

953   DAT (2000): Silurian - Lower Devonian black shales in Morocco: Where are the

954   organically richest horizons? J Petrol Geol 23:293-311

955

956   McPhail DC, Summerhayes E, Welch S, Brugger J (2003) The geochemistry of zinc

957   in the regolith. In: Roach IC (ed) Advances in Regolith. CRC for Landscape

958   Environments and Mineral Exploration, pp. 287–291

959

960   McPhail DC, Summerhayes E, Jayaratne V, Christy A (2006) Hemimorphite

961   solubility and stability of low-T zinc minerals. Geochim Cosmochim Acta 70:A414

962

963   Melcher F, Saini-Eidukat B, Göttlicher J, Steininger R, Cook N, Ciobanu C (2009)

964   Germanium in sphalerite and willemite at the Tres Marias mine, Mexico: An EMPA,

965   CL, LA-ICP-MS and synchrotron study. In: Hallesches Jahrbuch für

966   Geowissenschaften. DMG-Tagung 2009, Halle, pp. 163

967

968   Melchiorre EB, Enders MS (2003) Stable isotope geochemistry of copper carbonates

969   at the Northwest Extension deposit, Morenci district, Arizona: implications for

970   conditions of supergene oxidation and related mineralization. Econ Geol 98:607–621

971

972   Monteiro LVS, Bettencourt JS, Spiro B, Graca R, Oliveira TF (1999) The Vazante

973   zinc mine, Minas Gerais, Brazil: constraints on willemitic mineralization and fluid

974   evolution: Explor Min Geol 8:21–42

975

976   Monteiro LVS, Bettencourt JS, Juliani C, Oliveira TF (2006) Geology, petrography,

977   and mineral chemistry of the Vazante non-sulfide and Ambrosia and Fagundes

978   sulfide-rich carbonate-hosted Zn-(Pb) deposits, Minas Gerais, Brazil. Ore Geol Rev

979   28:201–234

980

981   Monteiro LVS, Bettencourt JS, Juliani C, Oliveira TF (2007) Nonsulfide and sulfide-

982   rich zinc mineralizations in the Vazante, Ambrosia and Fagundes deposits, Minas

983   Gerais, Brazil: Mass balance and stable isotope characteristics of the hydrothermal

984   alterations. Gondwana Res 11:362–381

985

986   Mouguina EM (2004) Les minéralisations polymétalliques (Zn–Pb, Cu, Co, Ni) du

987   Jurassique du Haut Atlas central (Maroc): Contexte géodynamique, typologies et

988   modèles génétiques. Dissertation, Faculté des Sciences Semlalia de Marrakech

989

990   O'Neil JR, Clayton RN, Mayeda TK (1969) Oxygen isotope fractionation in divalent

991   metal carbonates. J Chem Phys 51:5547-5558

992

993 Ouda B, El Hamdaoui A, Ibn Majah M (2005) Isotopic composition of precipitation at

994 three Moroccan stations influenced by oceanic and Mediterranean air masses. In:

995 Isotopic composition of precipitation in the Mediterranean Basin in relation to air

996 circulation patterns and climate. IAEA, Vienna, TECDOC-1453 pp 125-140

997

998 Palache C (1928) Phosphorescence and fluorescence of Franklin minerals. Am

999 Mineral 13:330–333

1000

1001 Palache C (1935) The minerals of Franklin and Sterling Hill, Sussex County, New

1002 Jersey. US Geol Surv Prof Pap 180, USGS, Washington

1003

1004 Pearce NJG, Perking WT, Westgate JA, Gorton MP, Jackson SE, Neal CR, Chenery

1005 SP (1997) A compilation of new and published major and trace element data for NIST

1006 SRM 610 and NIST SRM 612 glass materials. Geostand Newsl 21:115–144

1007

1008 Pokrovski GS, Roux J, Hazemann J-L, Testemale D (2005) An X-ray absorption

1009 spectroscopy study of argutite solubility and germanium aqueous speciation in

1010 hydrothermal fluids to 500 °C and 400 bar. Chem Geol 217:127-145

1011

1012 Pough FH (1940) Willemite morphology and paragenesis at Balmat, New York. Am

1013 Mineral 25:488-496

1014

1015 Pough FH (1941) Occurrence of willemite. Am Mineral 26:92–102

1016

1017 Randall JT (1938) Luminescence of solids at low temperatures. Nature 142:113–114

1018

1019   Rddad L, Bouhlel S (2016) The Bou Dahar Jurassic carbonate-hosted Pb-Zn-Ba

1020   deposits (Oriental High Atlas, Morocco): Fluid-inclusion and C-O-S-Pb isotope

1021   studies. Ore Geol Rev 72:1072–1087

1022

1023   Reichert J, Borg G (2008) Numerical simulation and a geochemical model of

1024   supergene carbonate-hosted non-sulphide zinc deposits. Ore Geol Rev 33:134–151

1025

1026   Rosenbaum J, Sheppard SMF (1986) An isotopic study of siderites, dolomites and

1027   ankerites at high temperatures. Geochim Cosmochim Acta 50:1147–1150

1028

1029   Rouvier H, Perthuisot V, Mansouri A (1985) Pb-Zn deposits and salt-bearing diapirs

1030   in Southern Europe and North Africa. Econ Geol 80:666–687

1031

1032   Saini-Eidukat B, Melcher F, Lodziak J (2009) Zinc-germanium ores of the Tres

1033   Marias mine, Chihuahua, Mexico. Mineral Depos 44:363–370

1034

1035   Saini-Eidukat B, Melcher F, Göttlicher J, Steininger R (2016) Chemical environment

1036   of unusually Ge- and Pb- rich willemite, Tres Marias Mine, Mexico. Minerals 6:20,

1037   doi:10.3390/min6010020

1038

1039   Sheffer HW (1966) The occurrence of germanium in willemite. Geochim Cosmochim

1040   Acta 30:837–838

1041

1042   Shore M, Fowler, AD (1996) Oscillatory zoning in minerals: A common

1043   phenomenon. Can Mineral 34:1111–1126

1044

1045   Spötl C, Vennemann TW (2003) Continuous-flow isotope ratio mass spectrometric

1046   analysis of carbonate minerals. Rapid Commun Mass Spectrom 17:1004–1006

1047

1048   Swart PK, Burns SJ, Leder JJ (1991) Fractionation of the stable isotopes of oxygen

1049   and carbon during reaction of calcite with phosphoric acid as a function of

1050   temperature and method. Chem Geol 86:89–96

1051

1052   Takahashi Y, Ando M, Iwasaki K, Masai H, Fujiwara T (2010) Defect activation in

1053   willemite-type Zn_2GeO_4 by nanocrystallization. Appl Phys Lett. doi:

1054   10.1063/1.3481081

1055

1056   Takesue M, Hayashi H, Smith RL (2009) Thermal and chemical methods for

1057   producing zinc silicate (willemite): A review. Prog Cryst Growth Char Mat 55:98–

1058   124

1059

1060   Terracciano R (2008) Willemite mineralisation in Namibia and Zambia. Dissertation,

1061   Università degli Studi di Napoli Federico II

1062

1063   Tsai MY, Yu CY, Wang CC, Perng TP (2008) Water-driven formation of luminescent

1064 Zn_2GeO_4 nanorods from Zn-containing Ge nanoparticles. Cryst Growth Des 8:2264–

1065   2269

1066

1067   Veizer J, Hoefs J (1976) Nature of O^{18}/O^{16} and C^{13}-C^{12} secular trends in sedimentary

1068   carbonate rocks. Geochim Cosmochim Acta 40: 1387−1395

1069

1070   Vivallo W, Broman C (1993) Genesis of the earthy ores at Garpenberg, south central

1071   Sweden. Geol Foren Stockh Förh 115:209–214

1072

1073   Yang P, Lu MK, Song CF, Liu SW, Gu F, Wang SF (2004) Photoluminescence of

1074 Pb^{2+} ions in sol–gel derived Zn_2SiO_4. Inorg Chem Comm 7:268–270

1075

1076   Zheng YF (1993) Calculation of oxygen isotope fractionation in anhydrous silicate

1077   minerals. Geochim Cosmochim Acta 57:1079–1091

Figure 1

a

Atlantic Ocean — Mediterranean Sea — Algiers — Tangier — Alpine Belts — Tell — Rif — Rabat — Middle Atlas — High Plateau — Moroccan Meseta — Saharan Atlas — High Atlas — **Bou Arhous deposit** — Anti Atlas — Saharan platform

0 125 250 km

b

N — S

"Grand Accident" Fault

Level 100
L. 50
L. 25
Level 0

$l_{1-2}m$
l_1b
l_1a
t
l_2m
l_4 — l_3

100 m

100 m

Mine dumps

Karst cavities

b
a
Ore veins
(a: sulfide, b: non-sulfide)

Marl and limestone (l_4)

Thin-bedded limestone (l_3)

Massive limestone ($l_{1-2}m$ & l_2m)

Saccharoidal limestone (l_1b)

Dolostone (l_1a)

Variegated shales (t)

Figure 2

Figure 3

a — Dissolved Quartz, Sparite, Micrite, Idiomorphic Quartz, 50 μm

b — Micrite, Dolomite, Quartz, Dol -> Cal, 100 μm

c — Sparite, Top of the series, Dolomite, Quartz, Micrite, 125 μm

Figure 4

Figure 5

Figure 6
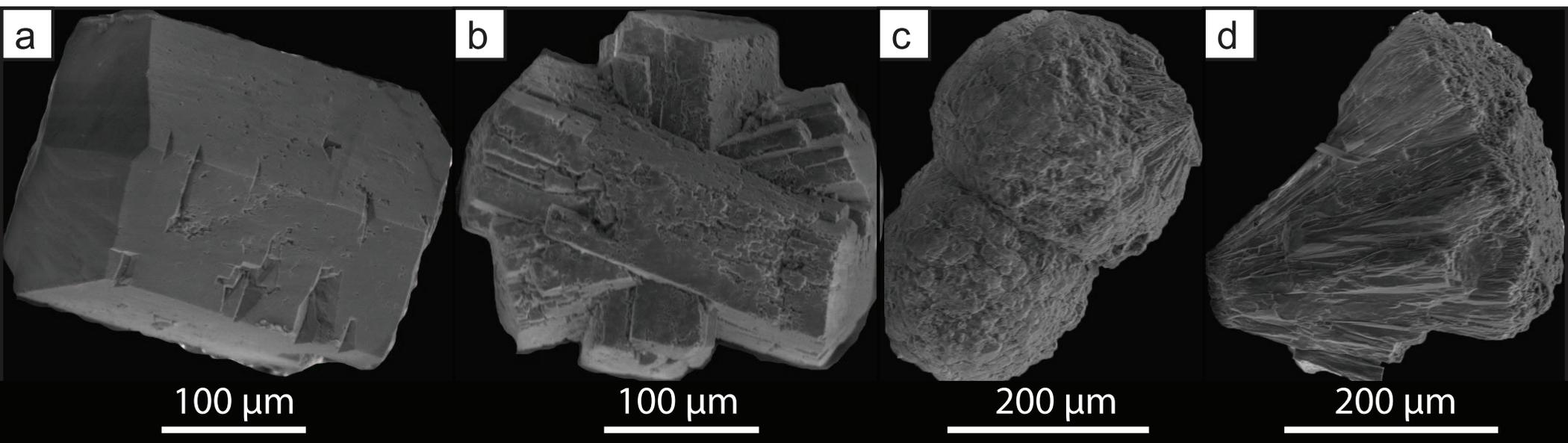
Figure 7

Figure 8

Figure 9

KARST FORMATION + NON-SULFIDE MINERALIZATION

DIAGENESIS

PRIMARY MINERALIZATION

ca. 195 Ma   ca. 190-185 Ma   from ca. 45 Ma

Limestone

Dolomite

Calcite

Quartz

Sphalerite

Galena

Willemite

Cerussite

Barite

Zn-clays

Dissolution

I   II

Ia   Ib   II

I   II   III

Figure 10

Figure 11

Legend:
- Zn$_2$SiO$_4$:xMn (x = 3*10^{-4})
- Zn$_2$SiO$_4$:xMn (x = 1.2*10^{-4})
- Zn$_2$SiO$_4$:xMn (x = 1.2*10^{-5})
- Zn$_2$SiO$_4$
- Zn$_2$GeO$_4$
- Wil Ia
- Wil Ib

Y-axis: Intensity (a.u.)

X-axis: Wavelength (nm)
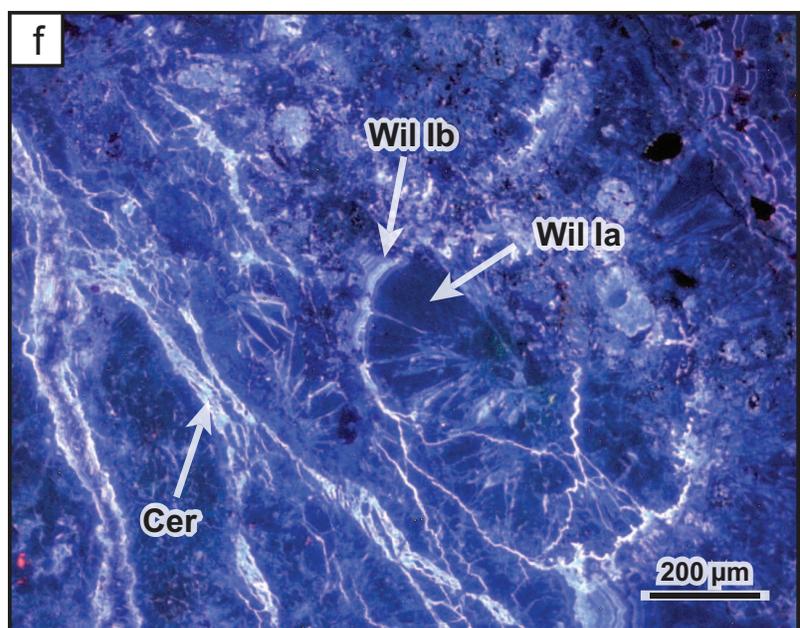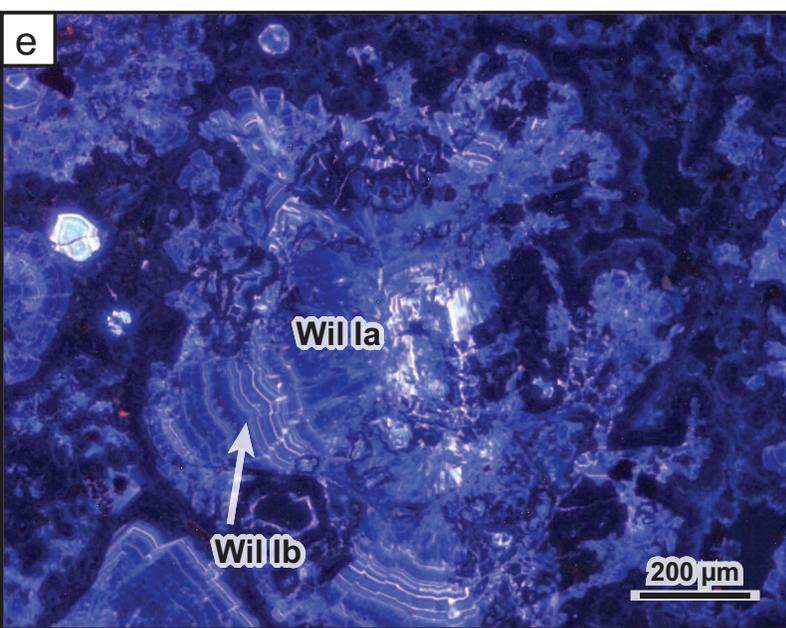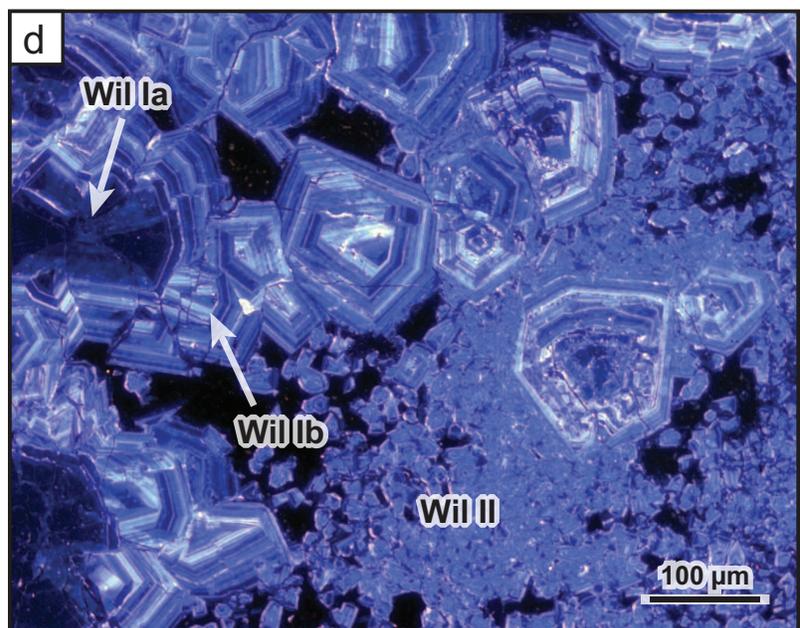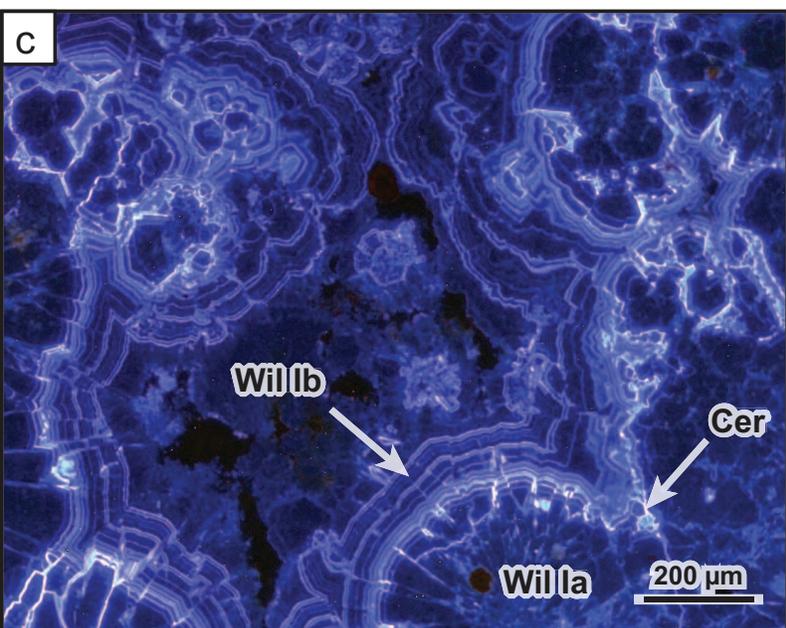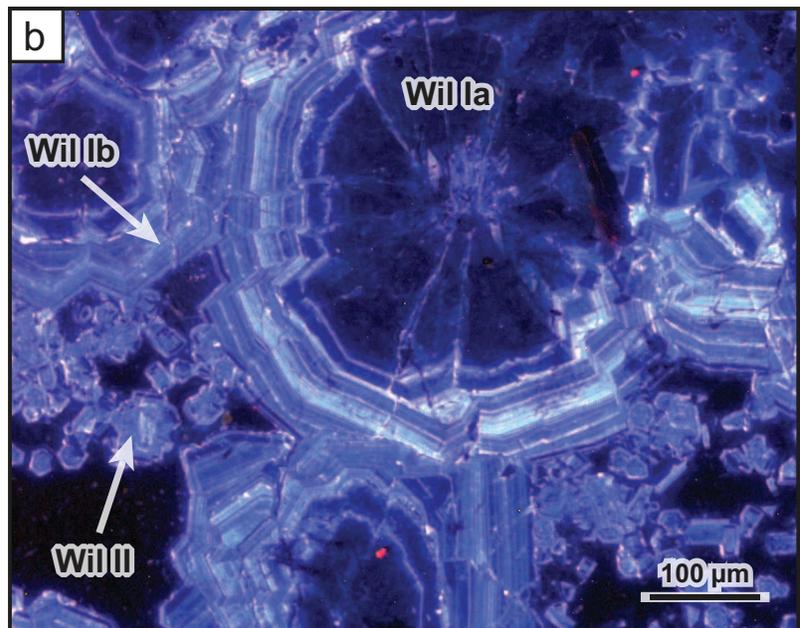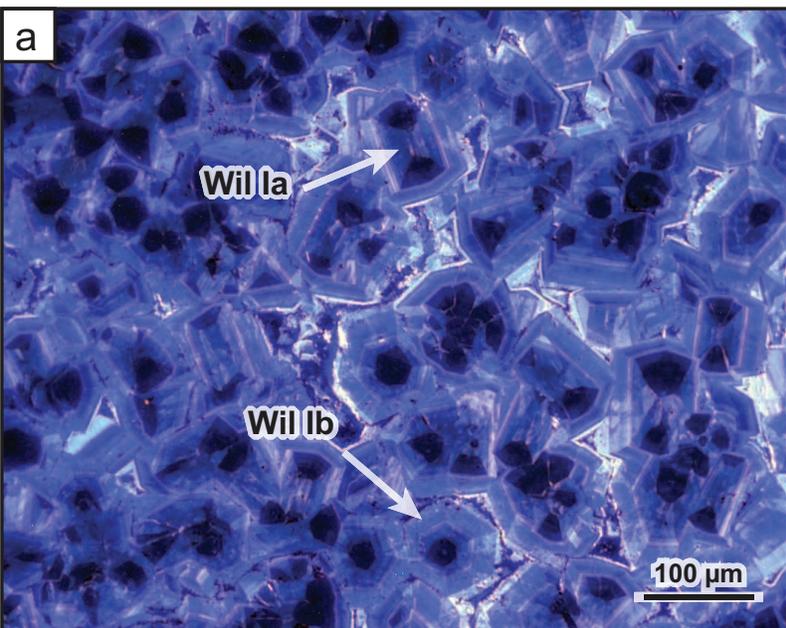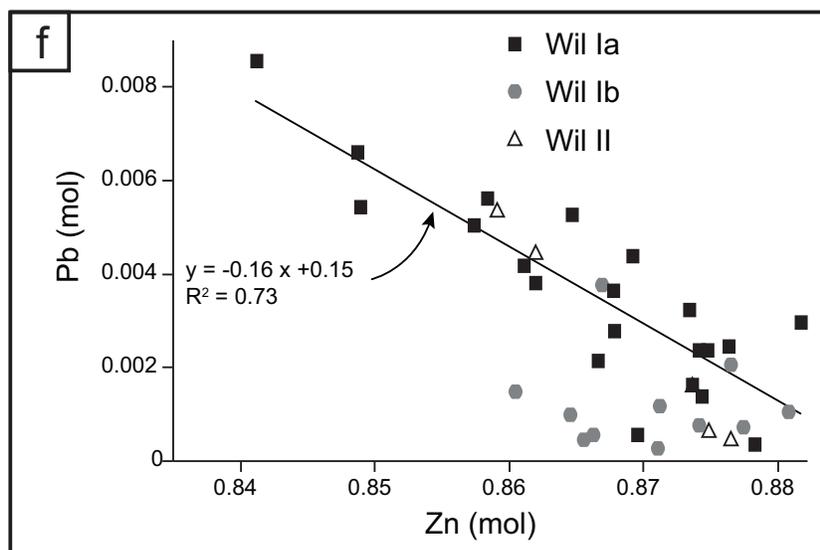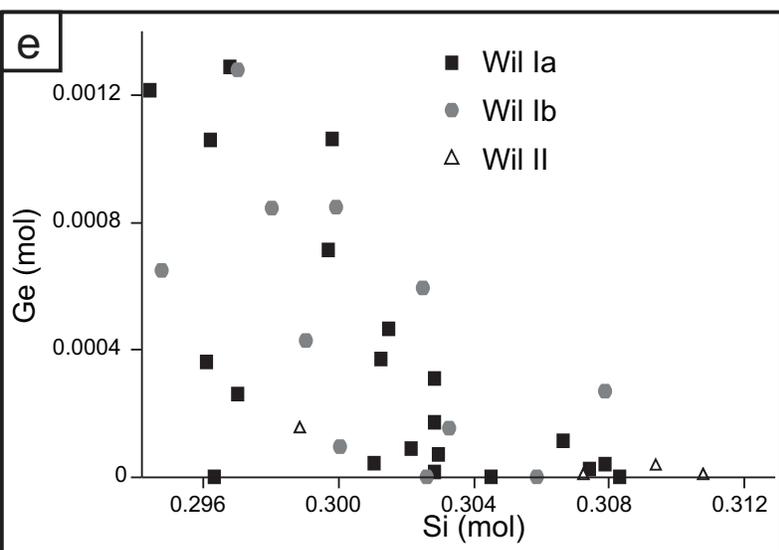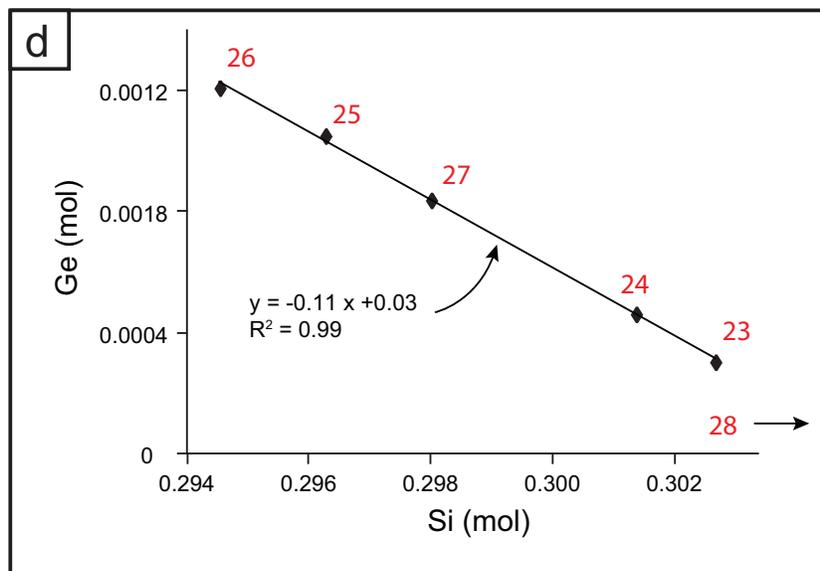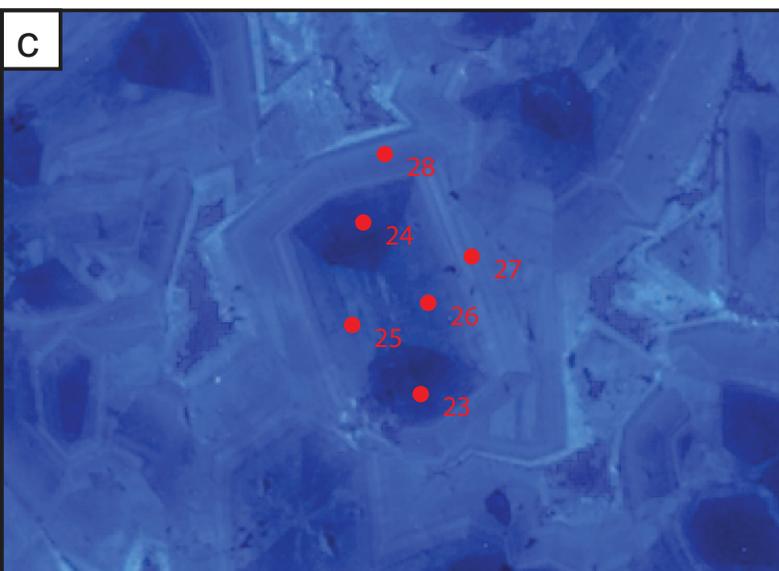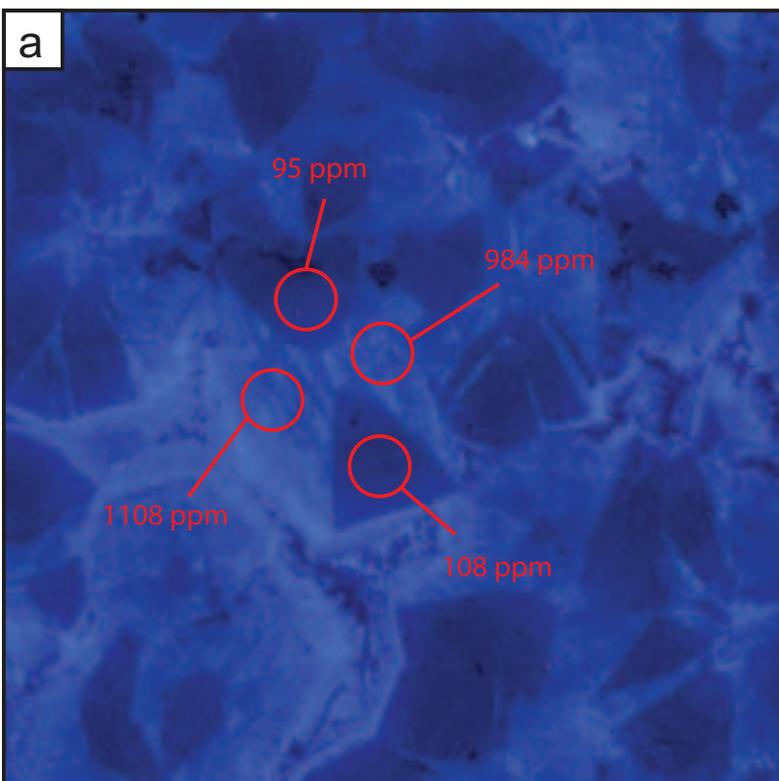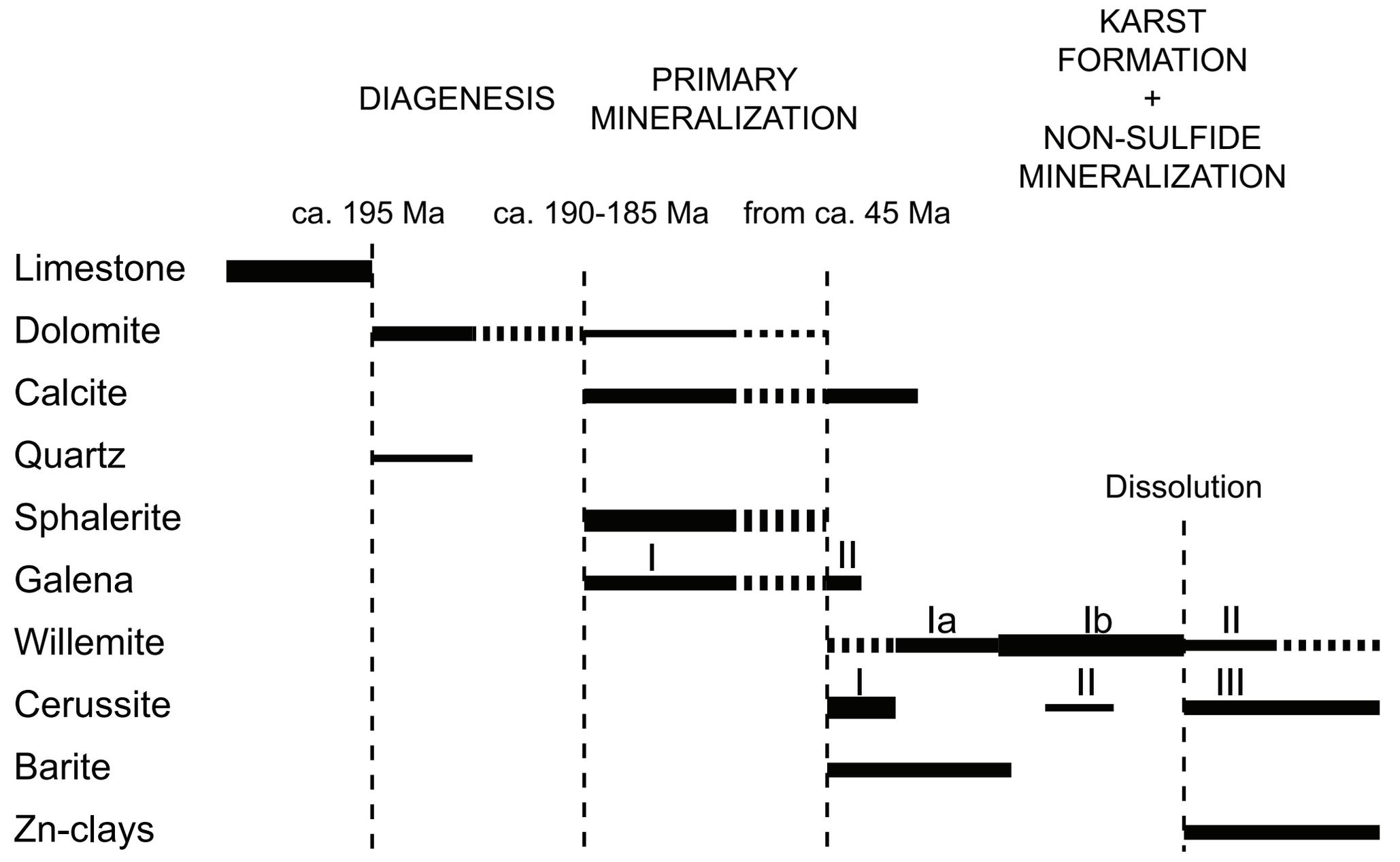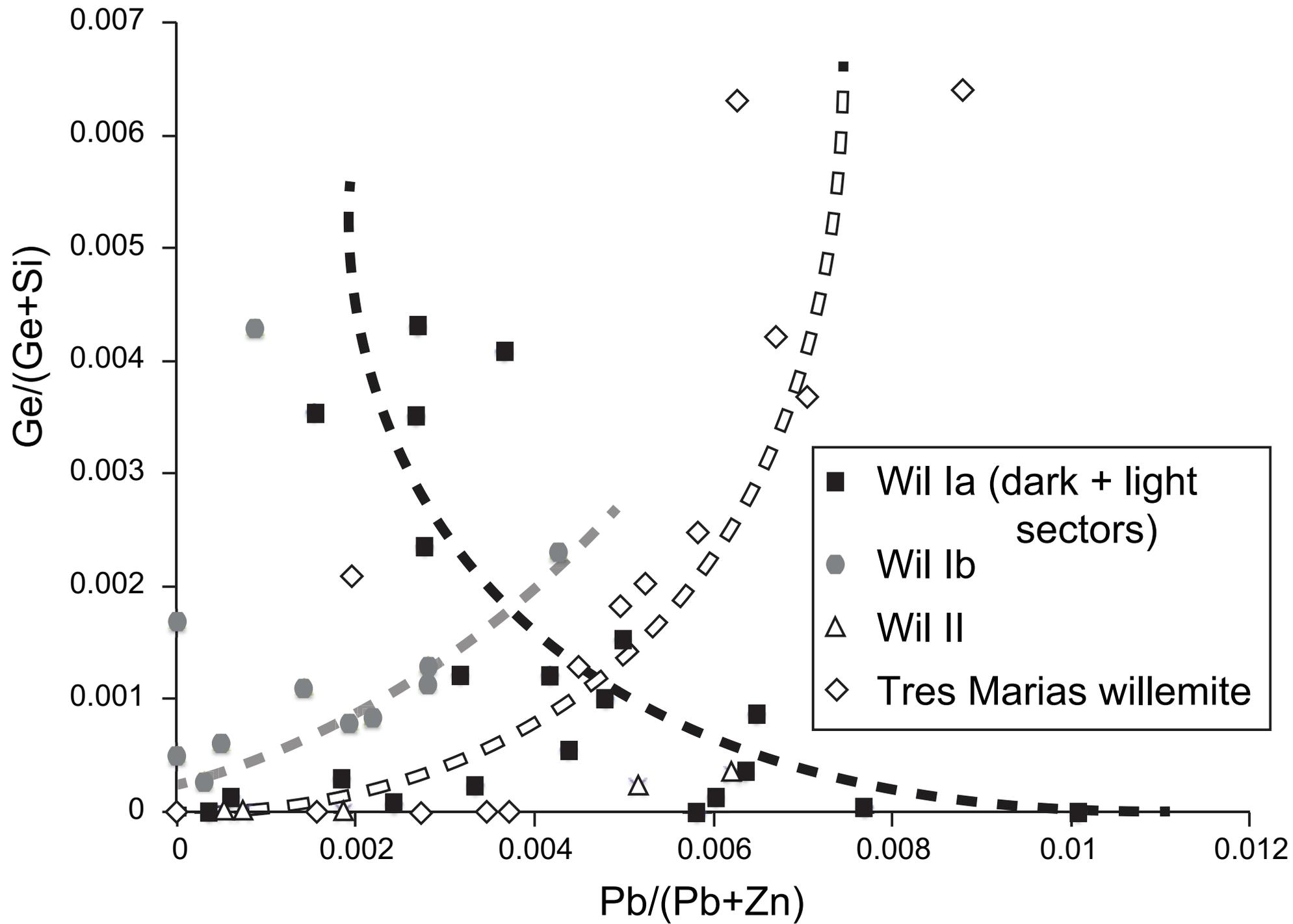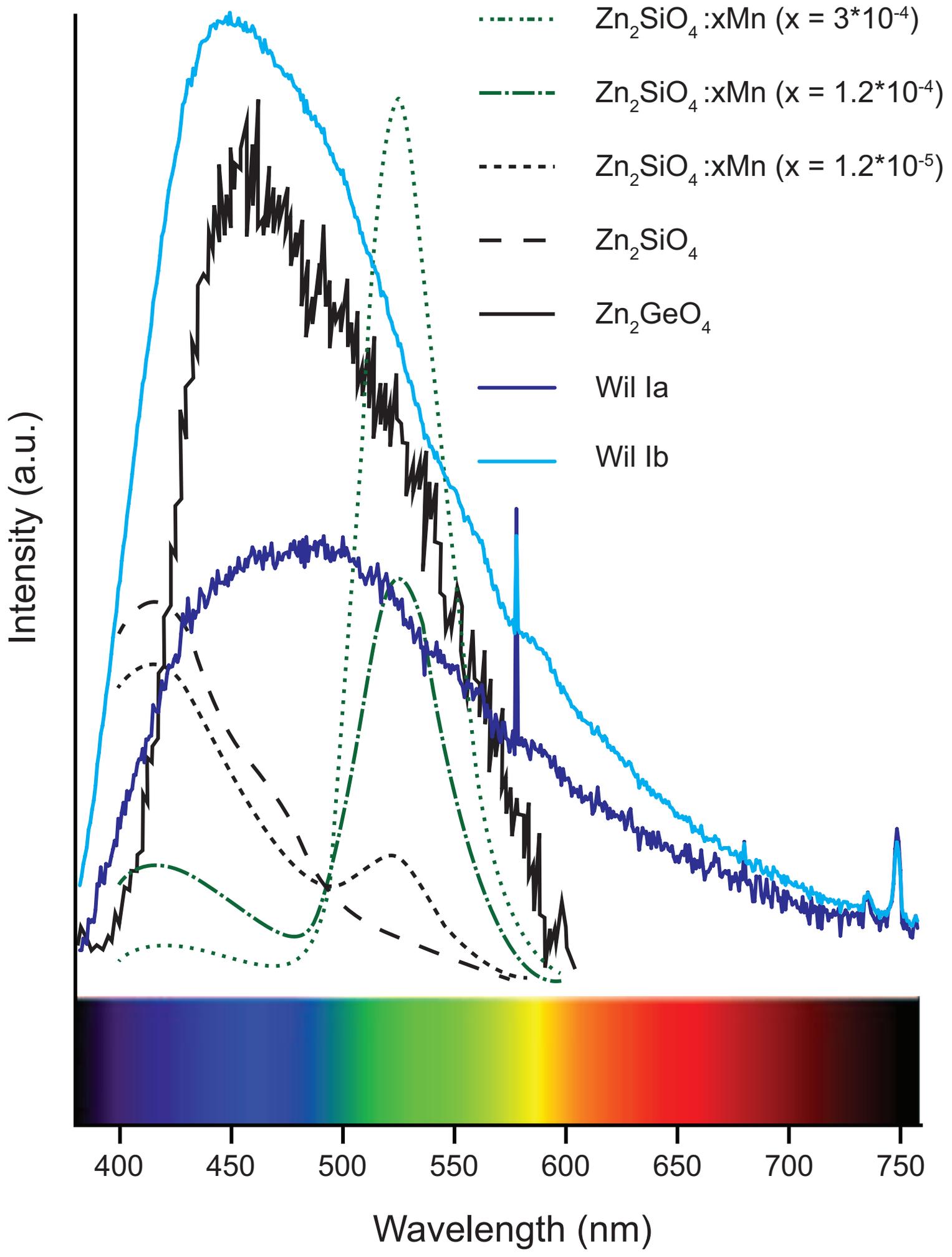
Figure 12
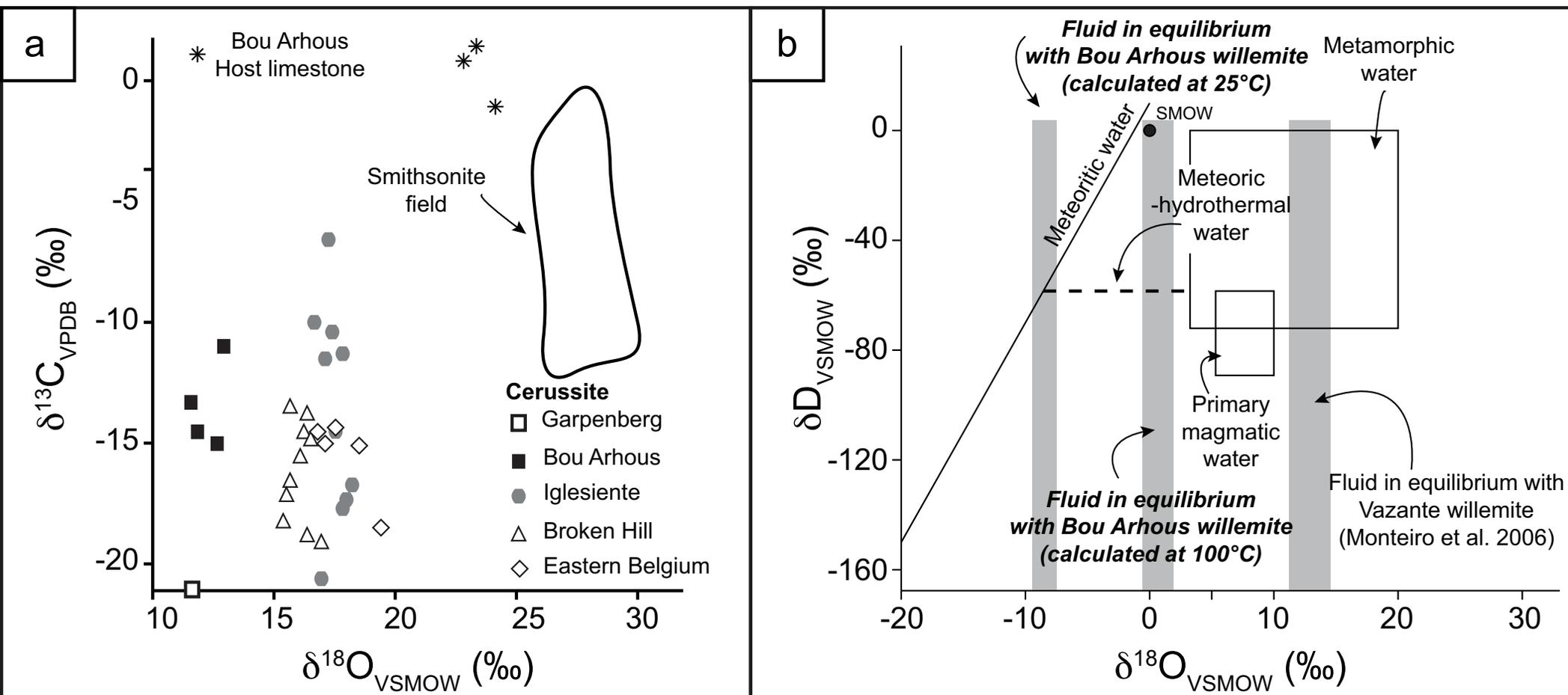
Table 1

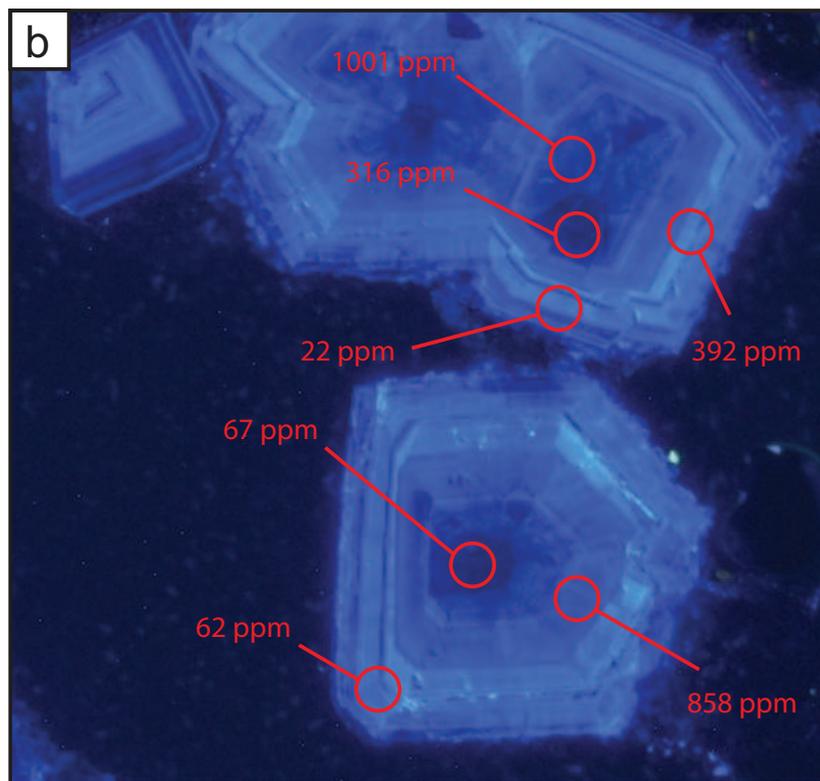| Sample	BA06A				BA06A			
Type	**Sphalerite n = 7**				**Sphalerite n = 14**			
	Range	**Avg.**	**SD**	**RSD**	**Range**	**Avg.**	**SD**	**RSD**
S	31.91-32.85	32.37	0.34	1	31.33-32.5	32.16	0.29	1
Cd	0.23-0.31	0.27	0.03	10	0.23-0.43	0.29	0.05	17
As	0-0.12	0.04	0.04	105	0-0.12	0.03	0.04	150
Bi	-				-			
Fe	0.04-0.07	0.05	0.01	19	0.04-0.21	0.09	0.04	39
Ag	0-0.06	0.02	0.02	119	0-0.15	0.04	0.05	139
Ni	0-0.02	0.01	0.01	94	0-0.02	0.01	0.01	115
Zn	65.1-66.44	65.85	0.49	1	65.12-66.52	65.878	0.4	1
Pb	-				-			
Ge	-				-			
Cu	0-0.1	0.01	0.01	96	0-0.1	0.01	0.02	175
∑	97.8-99.54	98.63	0.52	0.53	97.08-99.20	98.51	0.59	0.59

BA06A			
Galena n = 15			
Range	Avg.	SD	RSD
12.27-12.58	12.44	0.1	1
0.05-0.12	0.08	0.02	23
0-0.04	0.01	0.01	102
-			
0-0.02	0.01	0.01	142
0-0.29	0.04	0.09	230
0-0.02	0.01	0.01	172
0-0.03	0.01	0.01	142
86.32-87.43	86.91	0.38	1
-			
0-0.03	0.01	0.01	134
98.91-100.02	99.5	0.38	0.38

Table 2

Generation	Wil Ia (dark sectors) n = 15				
	Range	Avg.	SD	RSD	Range
SiO_2	27.29-28.36	27.89	0.31	1	27.12-27.60
GeO_2	0-0.05	0.03	0.01	33	0.04-0.13
Al_2O_3	0-0.07	0.04	0.02	50	0-0.02
ZnO	68.46-71.76	70.26	0.88	1	70.62-71.32
PbO	0.07-1.91	0.88	0.49	56	0.30-0.81
CdO	0-0.01	0.01	< 0.01	-	0-0.01
FeO	0-0.08	0.04	0.02	50	0-0.03
CaO	0-0.05	0.02	0.01	50	0-0.03
MnO	0-0.04	0.04	< 0.01	-	-
Total	97.75-100.31	99.11	0.60	1	98.78-99.54

Generation	Wil Ia (dark sectors) n = 5				
	Range	Avg.	SD	RSD	Range
Ge^{74}	108-316	177	82	46	825-1108

Generation	Wil Ib n = 11				
	Range	Avg.	SD	RSD	Range
SiO_2	27.15-28.32	27.71	0.33	1	27.75-28.69
GeO_2	0-0.13	0.06	0.04	67	0-0.01
Al_2O_3	0-0.06	0.03	0.02	67	0-0.09
ZnO	70.03-71.68	70.84	0.49	1	69.92-71.33
PbO	0.06-0.84	0.26	0.21	81	0.11-1.20
CdO	0-0.01	0.01	<0.01	-	-
FeO	0-0.04	0.03	<0.01	-	0-0.06
CaO	0.01-0.07	0.03	0.01	33	0-0.03
MnO	0-0.07	0.07	<0.01	-	0-0.04
Total	98.26-99.85	98.93	0.51	1	98.90-100.02

Generation	Wil Ib n = 3			
	Range	Avg.	SD	RSD
Ge^{74}	22-858	365	347	95

Wil Ia (light sectors) n = 5		
Avg.	SD	RSD
27.37	0.17	1
0.10	0.03	30
0.01	0.01	100
71.09	0.22	0
0.57	0.16	28
0.01	<0.01	-
0.03	<0.01	-
0.02	0.01	50
-	-	-
99.16	0.28	0

Wil Ia (light sectors) n = 9		
Avg.	SD	RSD
941	89	9

Wil II n = 5		
Avg.	SD	RSD
28.32	0.32	1
0.01	<0.01	-
0.04	0.03	75
70.74	0.58	1
0.56	0.45	80
-	-	-
0.06	<0.01	-
0.02	<0.01	-
0.04	<0.01	-
99.71	0.43	0

Table 3

Bulk cerussite

SAMPLE	δ^{13}C VPDB	δ^{18}O VSMOW
BA117	-11.0	12.9
BA118	-13.3	11.6
BA134	-14.5	11.9
BA153	-15.1	12.7

Host carbonates

SAMPLE	δ^{13}C VPDB	δ^{18}O VSMOW
BA147	-1.7	23.4
BA158	1.4	24.1
BA159	-1.0	22.9

Bulk willemite

SAMPLE	δ^{18}O VSMOW	δ^{18}O VSMOW	δ^{18}O VSMOW$_f^2$
BA117	7.8	-7.4	2.0
BA118	5.9	-9.3	0.1
BA124	5.3	-9.3	-0.5
BA128	5.9	-9.3	0.1
BA130	7.2	8.0	1.4
	7.0	-8.1	1.2
BA131	7.3	-7.8	1.5
BA133	6.9	-8.2	1.1
BA134	7.4	-7.8	1.6
BA135	6.4	-8.8	0.6
BA136*	*12.7*	*-2.5*	*6.9*
	12.5	*-2.7*	*6.7*
BA138	6.2	-9.0	0.4

*: BA136 contains a small proportion of quartz